

Inner Core Structure of Hurricane Alicia from Airborne Doppler Radar Observations

FRANK D. MARKS, JR.

Hurricane Research Division, NOAA/AOML, Miami, FL 33149

ROBERT A. HOUZE, JR.

Department of Atmospheric Sciences, University of Washington, Seattle, WA 98195

(Manuscript received 17 December 1985, in final form 17 November 1986)

ABSTRACT

Airborne Doppler radar measurements are used to determine the horizontal winds, vertical air motions, radar reflectivity and hydrometeor fallspeeds over much of the inner-core region (within 40 km of the eye) of Hurricane Alicia (1983). The reconstructed flow field is more complete and detailed than any obtained previously. The data show both the primary (azimuthal) and secondary (radial-height) circulations. The primary circulation was characterized by an outward sloping maximum of tangential wind. The secondary circulation was characterized by a deep layer of radial inflow in the lower troposphere and a layer of intense outflow above 10 km altitude. The rising branch of the secondary circulation was located in the eyewall and sloped radially outward. Discrete convective-scale bubbles of more intense upward motion were superimposed on this mean rising current, and convective-scale downdrafts were located throughout and below the core of maximum precipitation in the eyewall.

Precipitation particles in the eyewall rainshaft circulated 18–20 km downwind as they fell, consistent with the typical upwind slope with increasing altitude of eyewall precipitation cores. Outside the eyewall, the precipitation was predominantly stratiform. A radar bright band was evident at the melting level. Above the melting level, ice particles were advected into the stratiform region from the upper levels of the eyewall and drifted downward through a mesoscale region of ascent. Hypothetical precipitation particle trajectories showed that as these particles fell slowly through the mesoscale updraft toward the melting level, they were carried azimuthally as many as 1½ times around the storm. During this spiraling descent, the particles evidently grew vigorously. The amount of water condensed by the ambient mesoscale ascent exceeded that transported into the stratiform region by the eyewall outflow by a factor of 3. As the particles fell into the lower troposphere, they entered a mesoscale region of subsidence, the top of which coincided with the radar bright band.

1. Introduction

In a study of the structure of the developing eyewall of Hurricane Debby (1982), Marks and Houze (1984) demonstrated the ability of the National Oceanic and Atmospheric Administration's (NOAA) airborne Doppler radar to provide detailed mapping of the horizontal wind in tropical cyclones. In the present paper, we extend this work by considering a mature hurricane, as compared to the developing storm Debby, and by including analysis of the vertical wind as well as the horizontal wind. Our study focuses on the inner-core structure of Hurricane Alicia, which formed in the central Gulf of Mexico on 16 August 1983 and caused considerable damage in the cities of Galveston and Houston, Texas, when it moved onto land. [See Case and Gerrish (1984) for details of Alicia's track and development.] The domain of the analysis lies within 40 km of the storm center, while it was still offshore, and includes the eyewall and the immediately surrounding region of stratiform precipitation.

The present study utilizes the remote sensing capability of the airborne Doppler radar to determine the

three-dimensional wind field throughout the volume of space containing the hurricane's inner core. Previously, hurricane inner-core structure has been pieced together from in situ flight-level data obtained in many storms (Shea and Gray, 1973; Gray and Shea, 1973; Willoughby et al., 1982; Jorgensen, 1984a,b). The purpose of the present study is to construct as completely as possible the structure of the inner-core region of a single storm by examining the Doppler-derived three dimensional wind field together with the observed radar reflectivity pattern. By reconstructing the inner-core circulation from the Doppler radar data, we achieve the following major results.

(i) Inner-core structural features expected from previous compilations of flight-level data from many cases are confirmed to be present in a single, well-formed mature hurricane.

(ii) Features of the inner-core circulation that have been difficult or impossible to infer from traditional flight-level data—especially upper-level outflow from the eyewall and the lower-level convective downdrafts—are documented.

(iii) Recent theoretical studies of the dynamics of the inner-core region are confirmed.

(iv) Precipitation growth processes are revealed and components of the water budget of the inner-core region are determined.

2. Overall storm structure

Our study covers the period 0108–0200 UCT 18 August 1983. At this time, Hurricane Alicia was located near 28.5°N, 94.8°W (approximately 90 km south of Galveston, Texas) and was moving slowly ($<2 \text{ m s}^{-1}$) toward the west-northwest. Maximum winds at flight level (1500 m) were 50–53 m s^{-1} and the minimum central pressure was 967 mb.

Figure 1a shows the aircraft flight track (relative to the storm center) and the radar structure as viewed from the National Weather Service WSR-57 radar at Galveston. The aircraft track was obtained by plotting the aircraft position in a rectangular Cartesian grid with X positive to the east, Y positive to the north, and the origin (0, 0) located at the storm center. The storm track was determined objectively from the aircraft flight-level winds using the technique described by Willoughby and Chelmon (1982). The radar data from each sweep of the antenna were mapped into the Cartesian grid. Figure 1b is a schematic of the reflectivity pattern labeled using terminology developed by Willoughby et al. (1984b).

A well-developed eyewall was present during the time period under consideration. The strongest reflectivity in the eyewall was 40–42 dBZ along the northern semicircle at a radius of 12–15 km from the storm center. This region of strong reflectivity remained relatively fixed north of the storm center through the 52 min period of the analysis. Surrounding the eyewall, at a radius of 50–70 km from the storm center, was a large spiral-shaped “principal band” [Willoughby et al. (1984b)]. North and southwest of the eyewall, along the inside edge of the principal band were small, weaker rainbands connecting the principal band to the eyewall (Figure 1b). Willoughby et al. (1984b) hypothesized that these “connecting bands” contained mainly non-convective or stratiform precipitation.

Our study is confined to the boxes labeled 1 and 2 in Fig. 1a. Therefore, the eyewall and immediate surrounding region of lighter precipitation, including portions of the connecting bands, are examined. We do not consider the principal band in this study.

3. Data and methods of analysis

a. The airborne Doppler radar

The Doppler radar used in this study was installed on one of NOAA's two WP-3D research aircraft. The radar had a wavelength of 3.2 cm, peak power of 70 kw, a vertical beamwidth of 1.9° and a horizontal beamwidth of 1.35°. The antenna, located in the tail

of the aircraft (referred to as the “tail” radar), pointed at right angles to the aircraft's ground track while sweeping through elevation angles of 0°–360°. Thus, the Doppler radar, which responded to target velocity along the beam of the radar, measured the horizontal component of precipitation particle motion (or horizontal wind component) perpendicular to the flight track. When the antenna was not pointing horizontally, the vertical motions of precipitation particles also affected the measured velocity along the beam of the radar. When the antenna was pointing either directly upward or downward (vertical incidence), the vertical motion of particles was the only contribution to the measured velocity along the beam. The antenna rotated at a rate of one revolution per 7.5 s which provided data at all elevation angles once every 0.8 km of flight track.

The WP-3D aircraft also carried two non-Doppler, 5 cm wavelength, digital radars, one in the nose and one in the lower fuselage of the aircraft; however, data from these other two radars are not used in this study. More details of the characteristics of the radars aboard the aircraft are given by Jorgensen (1984a).

b. General procedures

The data obtained with the Doppler radar while the aircraft flew along legs 1–3 were used to determine the horizontal and vertical components of the wind in the inner core of the storm. The vector horizontal wind was reconstructed from the wind components measured along the beam of the radar while the aircraft was traversing two different flight legs. The vector wind in box 1 (cf. Figs. 1a and 2) was determined from the measured wind components perpendicular to legs 1 and 2 while the vector wind in box 2 was determined from components normal to legs 1 and 3. The vertical wind component along the flight track was determined from the data obtained while the antenna was at vertical incidence. A correction was made to the vertical-incidence data to remove the contribution of the particles' terminal fallspeeds. The remaining component was assumed to be the contribution of vertical air motion. The vertical wind component could not successfully be obtained by mass continuity from the horizontal wind field through boxes 1 and 2; this was probably due to errors introduced by the nonsimultaneity of measurement of the horizontal wind components from two different flight legs. The following subsections indicate more specifically how the radar data were analyzed to obtain the vertical velocity and the horizontal winds.

c. Analysis of vertical-incidence radar data obtained along flight legs 1–3

Vertical-incidence measurements along legs 1–3 of the flight track were used to construct radius–height

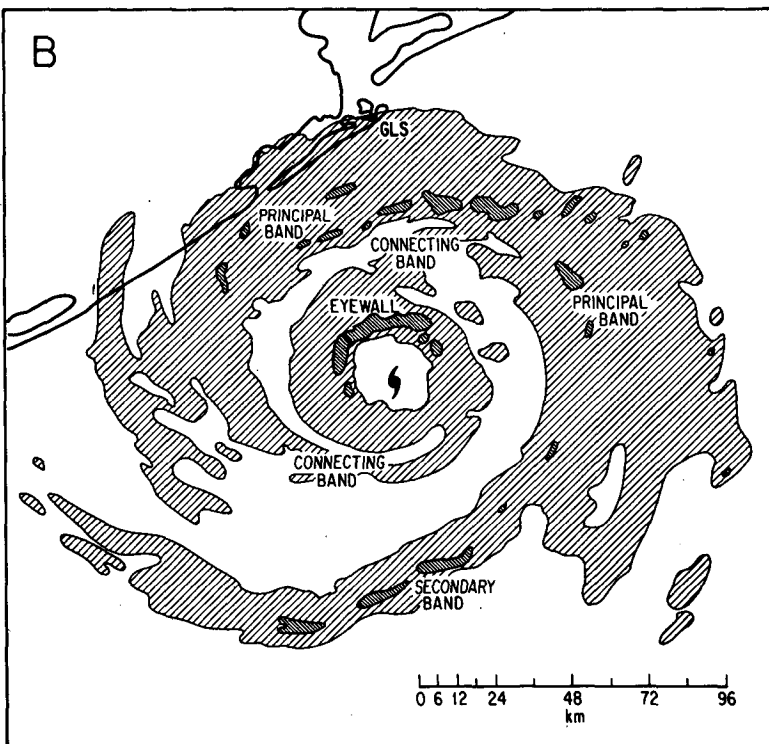
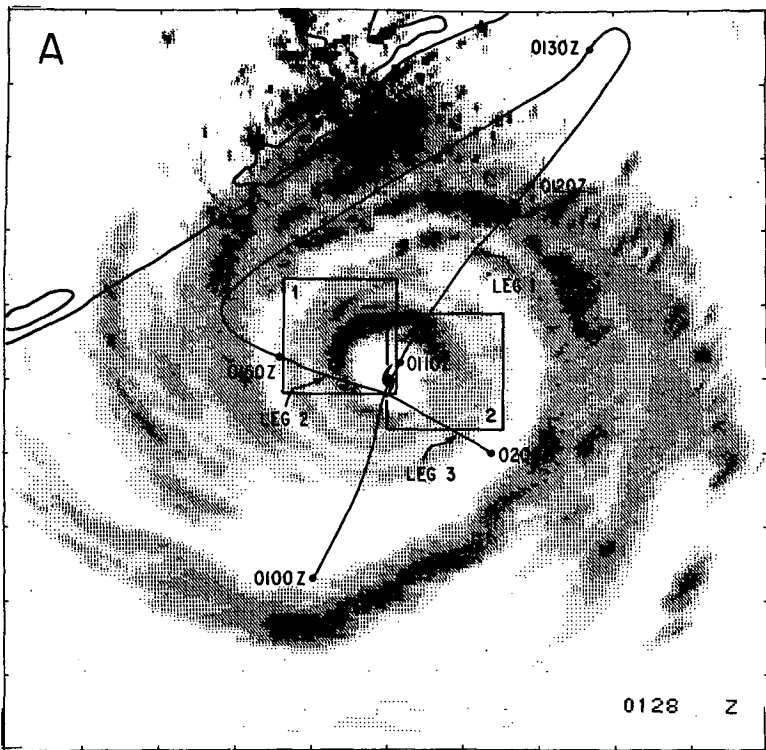


FIG. 1. (a) Horizontal distribution of reflectivity in Hurricane Alicia from the National Weather Service WSR-57 (10 cm) radar at Galveston, Texas, at 0128 UTC, 18 August 1983. Reflectivity contours are for 20, 25, 30, 35, and 40 dBZ. The aircraft flight track from 0100–0200 UTC is indicated by the solid line, and the analysis boxes, denoted by the thick solid line, are labeled 1 and 2. (b) Schematic of the precipitation features depicted in (a) showing the components of the stationary band complex as defined by Willoughby et al. (1984b). The contours are at 25 and 40 dBZ. The tick marks in (a) are 24 km apart. The Texas coastline is depicted by the solid line and the radar position at Galveston is labeled.

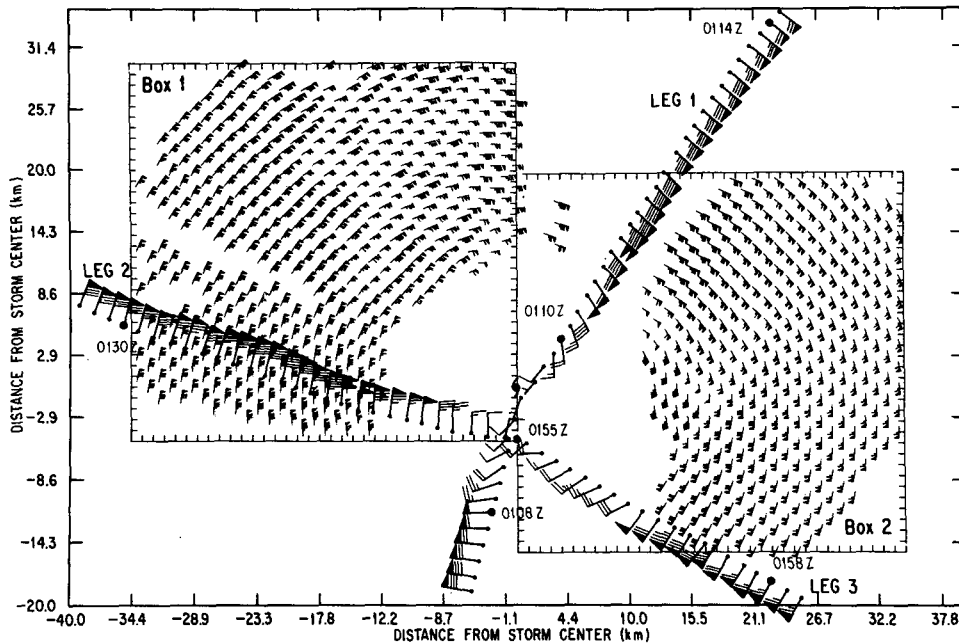


FIG. 2. Doppler-derived winds for boxes 1 and 2 at 1.2 km level and 1.5 level aircraft winds. The latter are plotted along flight tracks labeled in time (UTC). The wind plotting convention is flag, 25 m s^{-1} ; barb, 5 m s^{-1} ; and half-barb, 2.5 m s^{-1} . The hurricane symbol denotes the wind center derived from the flight-level data. The tick marks for the Doppler boxes are 1 km apart.

cross sections of reflectivity and vertical velocity (Figs. 3–6). The reflectivity cross sections were constructed by mapping all the reflectivity measurements into a radius–height grid with a vertical resolution of 300 m and a radial resolution of 1 km (Fig. 3). Radial distance from the storm center was determined by the objective technique of Willoughby and Chelmon (1982). When more than one reflectivity estimate was mapped to a particular grid element, the average reflectivity (Z in $\text{mm}^6 \text{ m}^{-3}$) was computed.

Vertical velocity cross sections were constructed by mapping the vertical-incidence Doppler velocities into a radius–height grid as previously discussed (Fig. 4). The vertical air velocity (w) was determined as a difference between the measured Doppler vertical velocity (W) and a bulk-estimate of the precipitation particle fallspeed, V_i :

$$w = W - V_i, \quad (1)$$

(Rogers, 1964). The mean terminal fallspeed of the precipitation particles was assumed to be a function of reflectivity and height; V_i (m s^{-1}) was estimated from Z ($\text{mm}^6 \text{ m}^{-3}$) as follows:

$$V_i = \begin{cases} 2.6Z^{0.107} & \text{for altitudes} < 5.1 \text{ km} \\ 0.817Z^{0.063} & \text{for altitudes} > 7.5 \text{ km} \end{cases}. \quad (2)$$

For altitudes between 5.1 and 7.5 km the two relations were combined linearly over the depth that melting occurred. This depth was determined from the vertical

gradient of Doppler vertical velocities in the altitude range 5.1–7.5 km. Lhermitte and Atlas (1963) were among the first to observe a sharp gradient in particle fallspeed at the altitude of the 0°C isotherm as ice particles melted. As can be seen in Fig. 4, there was a sharp decrease in W at 5.4 km, the approximate altitude of the 0°C isotherm. In the stratiform areas (radii 23–40 km) this jump occurred over a few hundred meters, whereas in the convective regions (radii 12–23 km) it occurred over a depth of 1.0–2.4 km. Hence, a minimum depth of 600 m was used to calculate particle fall-speeds in the stratiform regions, and in the convective regions the depth varied from 600 m to 2.4 km, depending on the strength of the velocity gradient observed.

The first of these empirical relationships is from Joss and Waldvogel (1970) and is for rain. The second formula was derived by Atlas et al. (1973) from the snow measurements of Gunn and Marshall (1958). These relationships are applicable at ground level. To apply these equations at other altitudes, they are multiplied by the density–height correction factor $[\rho_0/\rho(z)]^{0.45}$ suggested by Beard (1985) where $\rho_0 = 1.1904 \text{ kg m}^{-3}$, $\rho(z) = \rho_0 \exp[-z/9.58]$, and z is altitude in km. The density–height relationship was taken from Nuñez and Gray's (1977) composite Atlantic hurricane thermodynamic structure within 2° radius of the center.

The accuracy of the vertical velocities derived from this procedure is dependent on the accuracy of the Doppler radial velocities and the particle fallspeed

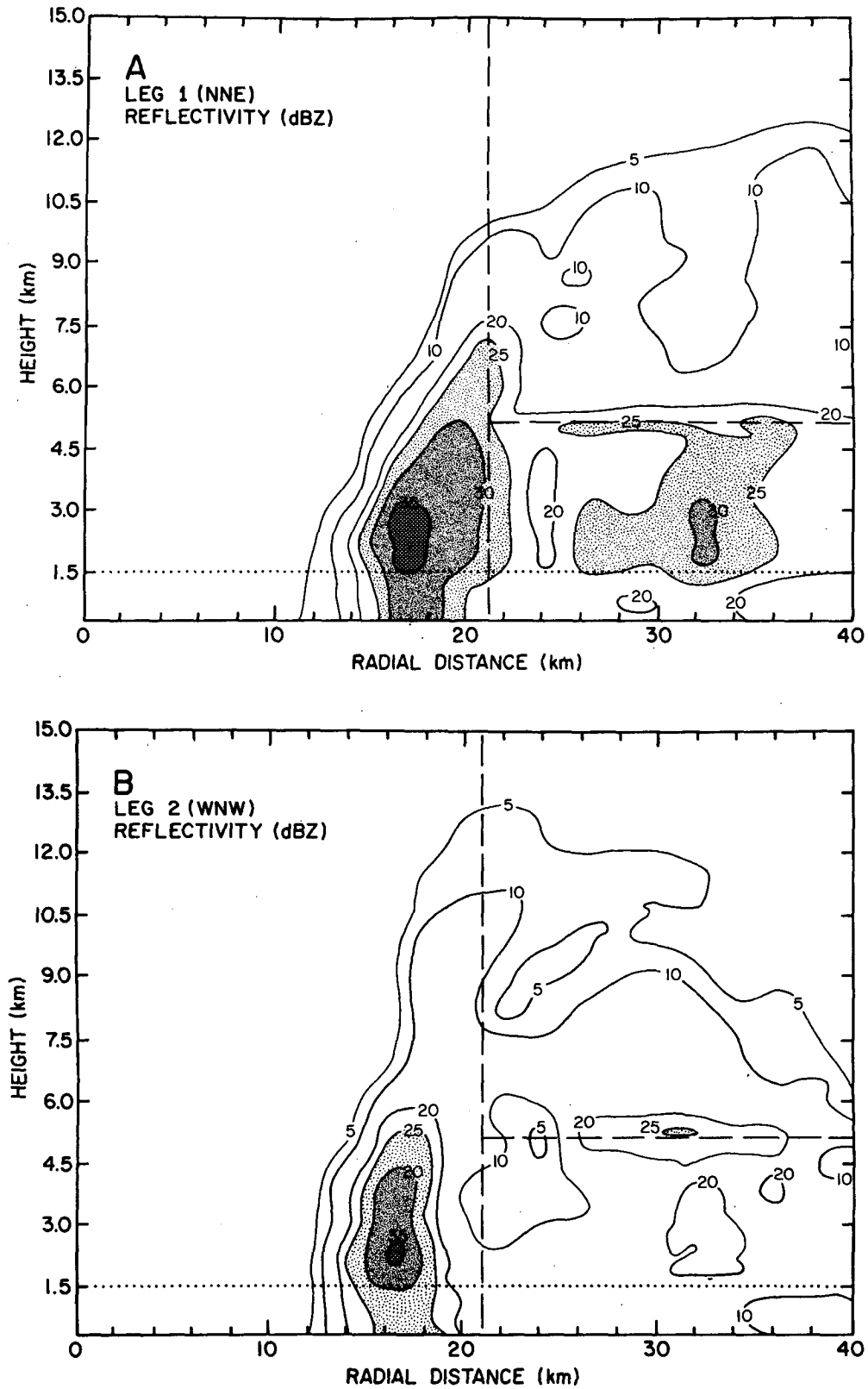


FIG. 3. Radius-height cross sections of reflectivity [dB(Z)] from the tail radar for (a) leg 1, (b) leg 2 and (c) leg 3. The aircraft flight level is depicted by the horizontal dotted line. The regions used to compute mean vertical velocities above and below the bright band are delineated in (a) and (b) by dashed lines.

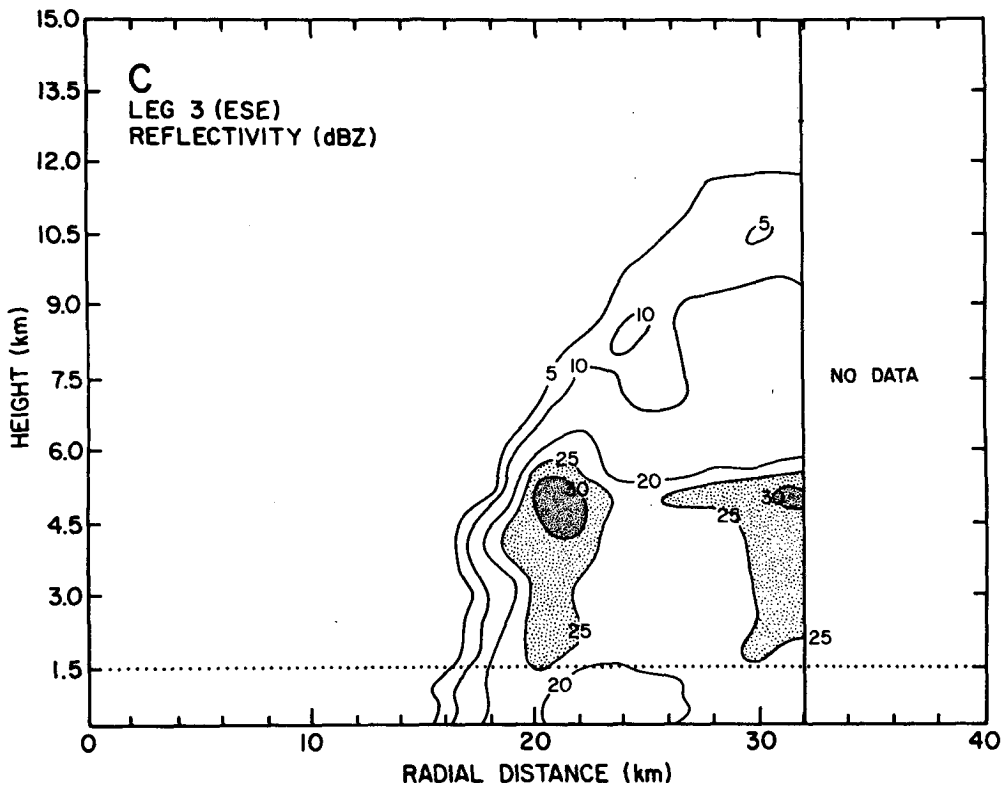


FIG. 3. (Continued)

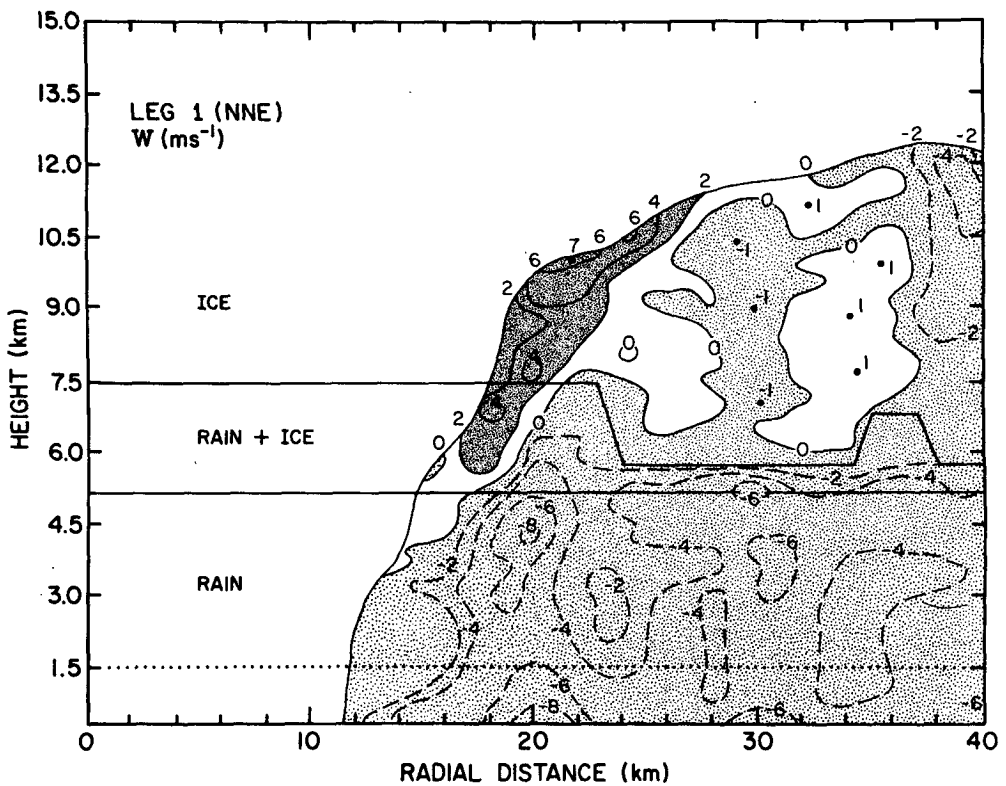


FIG. 4. Radius-height cross section of measured Doppler vertical velocity (W) for leg 1. The aircraft flight level is depicted by the horizontal dotted line. The altitudes used to partition the fallspeeds are indicated by thin horizontal lines. Regions of w exceeding 2 m s^{-1} are heavily shaded and regions of negative w are lightly shaded.

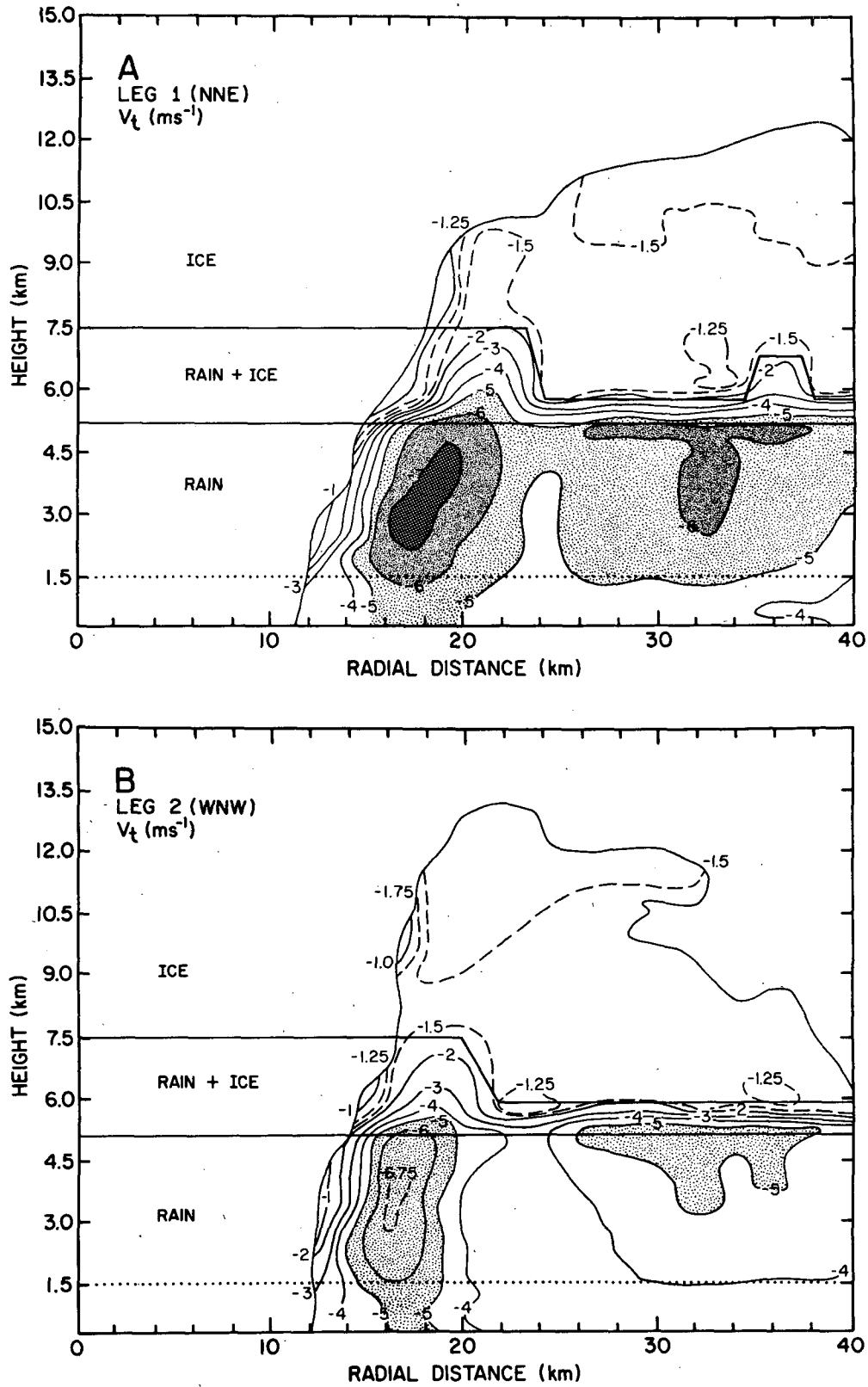


FIG. 5. Radius-height cross sections of mean particle fall speed (V_t , m s^{-1}) deduced from the tail radar reflectivity for (a) leg 1, (b) leg 2 and (c) leg 3. The aircraft flight level is depicted by the horizontal dotted line. The altitudes used to partition the fallspeeds are indicated by thin horizontal lines.

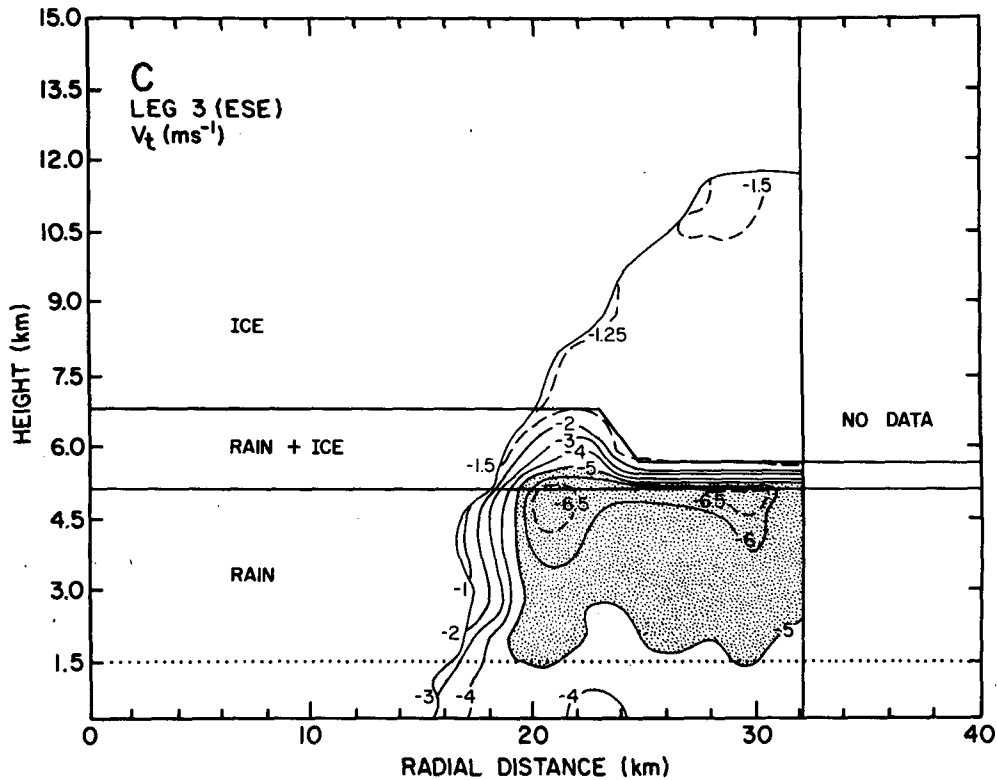


FIG. 5. (Continued)

computed. The accuracy of the Doppler radial velocities is $1.0\text{--}1.5\text{ m s}^{-1}$ (Jorgensen, et al., 1983; Marks and Houze, 1984). The particle fallspeeds vary very little in the ice ranging from $1.0\text{--}1.5\text{ m s}^{-1}$ for reflectivities of $5\text{--}20\text{ dBZ}$ (p. 377–346, Pruppacher and Klett, 1978). In rain, and in the convective regions in the vicinity of the melting layer, the particle fallspeeds vary the most: $1\text{--}3\text{ m s}^{-1}$ for low density graupel with reflectivities of $25\text{--}40\text{ dBZ}$, and $3\text{--}10\text{ m s}^{-1}$ for raindrops with reflectivities ranging from $20\text{--}45\text{ dBZ}$ (p. 322–328, Pruppacher and Klett, 1978). The desired accuracy of the vertical air velocity (w) is most critical in the stratiform regions where w is smaller than the particle fallspeed and the uncertainty in the Doppler radial velocity. Hence, w 's in the stratiform areas have been averaged in time (radius) to diminish the uncertainty in estimating the weaker mesoscale motions. In the convective regions, the magnitude of the vertical motions is typically larger than the uncertainties in the velocity estimates.

d. Analysis of horizontal winds and reflectivity in boxes 1 and 2

Dual-Doppler synthesis of the horizontal winds in the regions within the boxes labeled 1 and 2 in Fig. 1 was carried out following, generally, the procedure

outlined by Marks and Houze (1984) and Jorgensen et al. (1983). In these studies, w and V_t were assumed to be zero and the horizontal wind components (u and v) were directly determined from the Doppler velocity estimates along the beam. Here, however, the technique has been modified to include the effect of w and V_t in the solution for the horizontal wind components; V_t was estimated from the instantaneous reflectivity estimates (as described in Sec. 3c) and w was determined from (1). The Doppler velocity estimates along the beam, corrected for fallspeed, were then used to estimate u and v following Jorgensen et al. (1983).

In principle, a further refinement could be achieved by integrating the continuity equation to obtain w from the estimated u and v fields. The measured velocity components along the radar beam could then also be corrected for w and new u , v field computed. This procedure could be repeated until the u , v and w values converged. However, we found that the separation in time of the Doppler velocity estimates from the three flight legs was too great to obtain divergence fields that were accurate enough to calculate w reliably at all points in the analysis domain.

As noted in section 3a, horizontal wind fields for the two boxes were constructed from the Doppler radar data obtained on the southwest–northeast flight path (0108–0115 UTC leg 1) and the northwest–southeast leg (0148–0200 UTC, legs 2 and 3). The grid elements

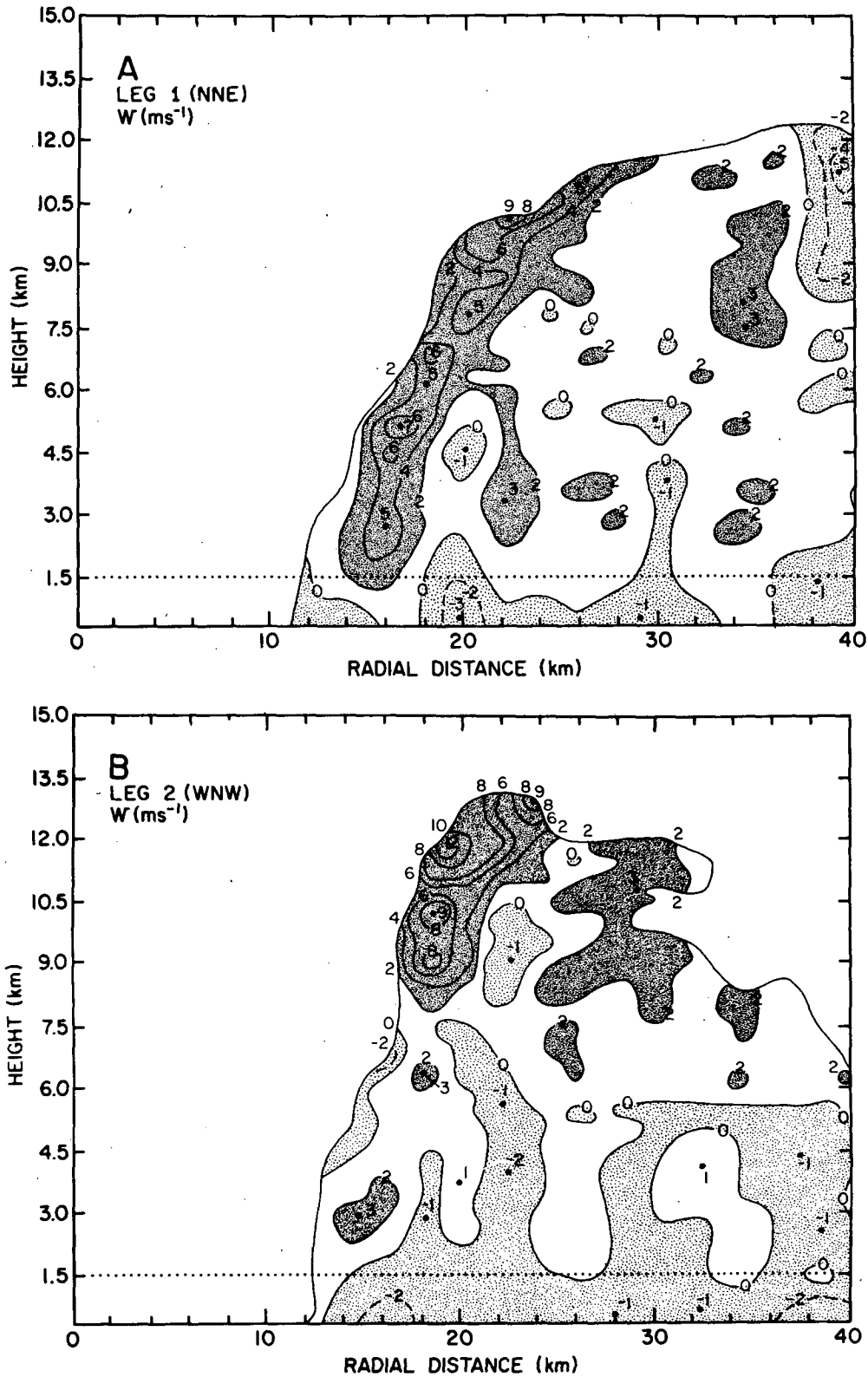


FIG. 6. Radius-height cross sections of vertical velocity (w , m s^{-1}) from tail radar for (a) leg 1, (b) leg 2 and (c) leg 3. The aircraft flight level is depicted by the horizontal dotted line. Positive w is denoted by thin solid lines and negative w by thick solid lines. Regions of w exceeding 2 m s^{-1} are heavily shaded and regions of negative w are lightly shaded.

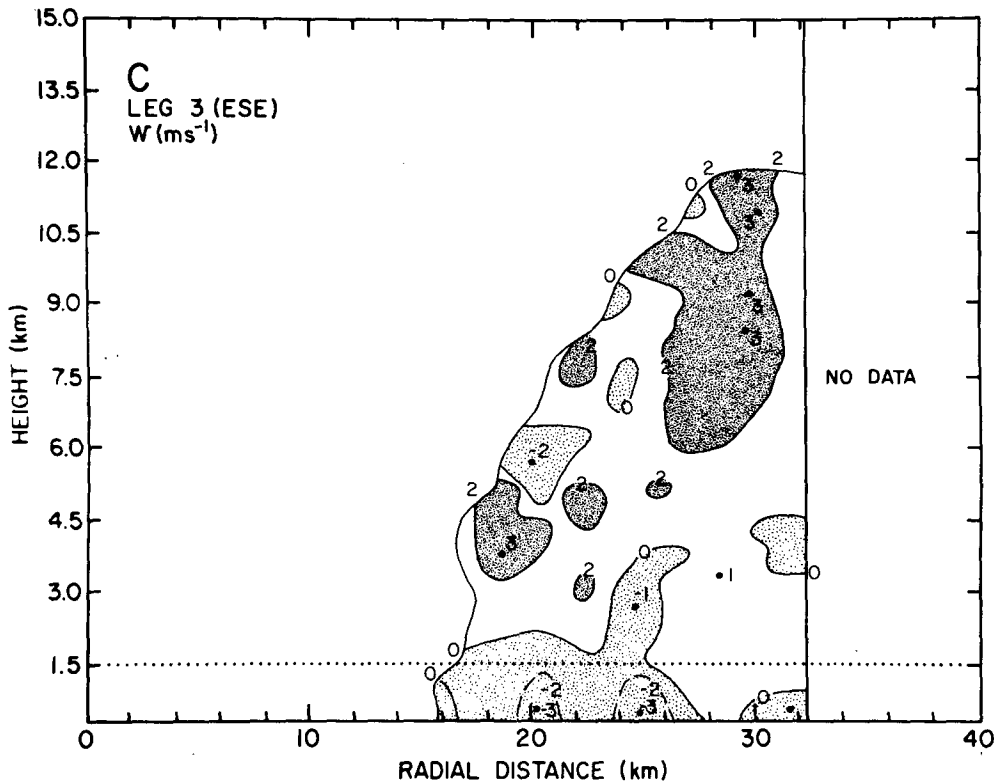


FIG. 6. (Continued)

used in the two analyses were $1 \text{ km} \times 1 \text{ km}$ in the horizontal and 0.7 km in the vertical starting at 0.5 km altitude. These flight legs had ideal viewing angles for dual-Doppler synthesis of winds in boxes 1 and 2, since the legs were nearly perpendicular.

The quality of the Doppler-derived horizontal winds was examined by comparing the Doppler-derived winds at the 1.2 km level with the aircraft winds measured along the flight tracks at an altitude of 1.5 km . Doppler-derived horizontal wind fields for boxes 1 and 2 at 1.2 km altitude are shown with the 1.5 km flight level winds in Fig. 2. The box 1 and 2 winds are in very close agreement with the flight-level aircraft winds (directions $\pm 3\text{--}4^\circ$ and speeds $\pm 1\text{--}2 \text{ m s}^{-1}$), and give a clear representation of the wind circulation around the vortex core.

Within the analysis boxes, three-dimensional, time-composite reflectivity patterns were also constructed from the tail radar reflectivity data in the manner described by Marks and Houze (1984). The grid elements used were identical to those used in the wind analysis.

4. Observed inner-core structure

a. Results of analysis of vertical-incidence radar data

Figures 3, 5, and 6 show the radius–height cross sections of reflectivity, mean particle fallspeed and vertical

velocity, respectively, along legs 1–3 of the flight track shown in Fig. 1a. The cross sections clearly delineate the two types of precipitation regimes discussed by Jorgensen (1984a,b) and Marks (1985) in studies of Hurricane Allen and other storms: 1) a convective regime in the eyewall; and 2) a nonconvective or stratiform regime farther from the storm center outside the eyewall.

The eyewall was identified in vertical cross sections as a lower-tropospheric column of high reflectivity. The reflectivity contours making the inner edge of the eyewall sloped radially outward with height (Figs. 3a–c). This inclined structure has been observed in other hurricanes (Jorgensen, 1984a,b; Marks, 1985). Peak values of $30\text{--}38 \text{ dBZ}$ lay $2\text{--}4 \text{ km}$ above the sea surface. The column of high reflectivity ($\geq 20 \text{ dBZ}$) generally did not extend much above $6\text{--}7 \text{ km}$. The estimated terminal fallspeeds of precipitation particles in the region of the low-tropospheric peak of reflectivity were $6\text{--}7 \text{ m s}^{-1}$. These high values are characteristic of heavy rain. Above 5.1 km , the values of V_t in the eyewall dropped off abruptly to values of $1.0\text{--}1.5 \text{ m s}^{-1}$. This transition occurred at the heights where the reflectivity (from which V_t was calculated) decreased abruptly to lower values and where the fall-velocity relationship for ice in (2) was combined linearly with that for rain, thus yielding a lower fallspeed for any given reflectivity.

The maximum updraft velocities in the eyewall were located in a pattern of bubbles along the sloping border of the echo pattern which were strongest above 8 km altitude in the ice region. Maximum values were $>5 \text{ m s}^{-1}$. If the w pattern consisting of discrete cores was smoothed, mean slantwise ascent would be seen to follow the inner border of the echo. This core of mean ascent would lie inside and just above the eyewall reflectivity maximum apparent in Figs. 3a–c. Similar juxtapositions of updraft and reflectivity maximum were described by Jorgensen (1984a,b) and Marks (1985). This observation suggests a general picture in which precipitation particles forming in a continual series of convective bubbles successively rising in a general slantwise flow fell out into a precipitation shaft that produced the eyewall reflectivity maximum situated outward at and just below the sloping time-mean updraft. This interpretation is discussed further in section 5b.

Convective-scale downdrafts were also associated with the eyewall reflectivity pattern. These features had peak absolute values of $3\text{--}4 \text{ m s}^{-1}$ near the ocean surface and were located throughout the region within and below the eyewall rainfall maximum.

The nonconvective region, outside the eyewall, was more homogenous horizontally and had stratified structure (Figs. 3 and 5). The reflectivity pattern was characterized by a bright band at the melting level (4.8 km). Both reflectivity and particle fallspeed decreased sharply above that altitude, where the precipitation was predominantly ice. The magnitude of the reflectivity in the bright band was 25–30 dBZ.

The vertical air motions in the nonconvective region were weaker than those in the eyewall (Fig. 6). The vertical velocity pattern was stratified with generally weak downward motion (peaks of $2\text{--}3 \text{ m s}^{-1}$) below the bright band, and weak ascent (peaks of $2\text{--}3 \text{ m s}^{-1}$) above the bright band. As in the eyewall, the peak downdrafts were correlated with the local reflectivity maxima.

Above 6 km in the nonconvective region, there is one region of downdraft associated with a weak reflectivity maximum seen along leg 1 at 10 km altitude and 36 km radius. This downdraft may be an artifact that results from an underestimation of V_i in the reflectivity maximum. The hydrometeors may have been small graupel, that were advected out of the eyewall somewhere upwind, and have a slightly different V_i – Z relationship from that used in (2). Another type of fallspeed estimation problem may have affected the w calculations at low levels in the nonconvective region, especially in the lowest levels near the sea surface. At these levels, Figs. 6a–c show $1\text{--}4 \text{ m s}^{-1}$ downdrafts extending out to 30–40 km radius. The reflectivity in this area (Fig. 3a) was lower than in the region just above, resulting in a drop in V_i . The dropsize distribution at flight level (1.5 km) in this region (not shown) indicated that while the number of hydrometeors decreased in

this region, their median diameters stayed the same. Radar reflectivity (Z) is a function of both the number of hydrometeors in a volume and their diameter, while the actual V_i of precipitation particles is a function of particle diameter only. Therefore, when the number of hydrometeors decreased, the reflectivity decreased, leading to a decrease in calculated V_i . However, the diameters of the hydrometeors stayed the same, indicating the actual V_i remained more nearly constant. Thus, the downdraft strength was overestimated.

Average vertical velocities were calculated from the first two cross sections in Fig. 6 for regions above and below the bright band (delineated in Fig. 3) to determine the magnitude of the mesoscale mean up- and down-motions. Average vertical velocities were not computed for leg 3 because the data did not extend far enough in range. In the cross section shown in Fig. 6a, the mesoscale average downward velocity was -0.1 m s^{-1} (standard deviation of 1.1 m s^{-1}) and the mesoscale average upward motion was 0.8 m s^{-1} (standard deviation of 1.9 m s^{-1}). In the cross section shown in Fig. 6b, the average mesoscale up- and downdraft were a little stronger than those in Fig. 6a: -0.3 m s^{-1} (standard deviation 0.9 m s^{-1}) below the bright band and 1.3 m s^{-1} (standard deviation 1.6 m s^{-1}) above. The sign and magnitude of the vertical motions above and below the bright band in leg 3 were consistent with those in the other two legs. The values of mesoscale ascent and descent in the cross sections appear to be larger than those deduced for the stratiform rain areas associated with tropical squall lines (e.g., Leary and Houze, 1979; Gemache and Houze, 1983; Houze and Rappaport, 1984).

The greatest uncertainty in the determination of the w fields (Fig. 6) is in the calculation of V_i (discussed in sec. 3c). The values of V_i in Fig. 5 seem entirely consistent with the fall velocity data described by Pruppacher and Klett (1978). However, if, for example, the values of V_i computed by (2) had a bias of 25 or 30%, then the results just described might be altered. A bias of this magnitude would not affect the result that a mesoscale updraft exists above the melting layer, since at those levels the values of V_i are generally small. However, at lower levels, a 25–30% bias in values of V_i for rain could lead to $1\text{--}2 \text{ m s}^{-1}$ uncertainty in the vertical air velocity w . Thus, the mesoscale downdraft inferred to exist below the melting layer in the stratiform region could be weaker than indicated. Nonetheless, our best estimate remains that a mesoscale downdraft was present below the melting layer.

The radius–height cross sections also indicate several asymmetric features of the eyewall and its surrounding stratiform region. In the eyewall, legs 1 and 2 (Figs. 3a–b and 6a–b), in the front quadrant of the storm, had larger reflectivity and stronger velocity peaks than did leg 3 (Figs. 3c and 6c), which was in the rear quadrant of the storm. The strongest reflectivity peaks in the stratiform region below the bright band were in

legs 1 and 3, counterclockwise or upwind of the peak reflectivity in the eyewall (Figs. 3a and 3c). The stratiform portion of leg 2 (Fig. 3b), just downwind and radially outward of the largest reflectivity in the eyewall (Fig. 1), had smaller reflectivity than that in the legs on the side of the storm with the smaller eyewall reflectivity. The downward vertical velocity below the bright band was strongest in legs 2 and 3, downwind of the portion of the eyewall with larger reflectivity and stronger vertical velocity. The downward vertical velocity below the bright band was weakest in leg 1, upwind of the strongest portion of the eyewall. These asymmetric features of the storm are discussed further in Sec. 5d.

b. Tangential and radial wind structure in boxes 1 and 2

Figures 7 and 8 show the radius–height cross sections of the tangential and radial components of the horizontal wind field (V_θ and V_r) derived from the three-dimensional wind analysis within the regions of boxes 1 and 2 (Fig. 1). To obtain these cross sections, the Doppler-derived vector horizontal winds at each grid point were resolved into V_θ and V_r components and mapped into 2 km wide radial bins. The data mapped into each radial bin were then averaged.

The resulting mean tangential wind field (Fig. 7) exhibited a radially outward sloping region of maximum values, with strongest winds at low levels (1.5–2.5 km in both boxes) and stronger flow on the northwest side of the storm (box 1). The tangential wind maximum was located radially just outside the radar reflectivity maximum and its outward slope with height was larger than that of the reflectivity or vertical velocity maxima (cf. Figs. 3, 6 and 7). The slope of the tangential wind maximum and its general location relative to the reflectivity and vertical velocity maxima are consistent with numerical model results (Willoughby et al., 1984a, see especially their Fig. 8) and composites of flight-track wind data (Willoughby et al., 1982; Jorgensen, 1984b). Shea and Gray's (1973) results, however, suggest that the radius of maximum wind does not slope outward in more intense storms. Their study is the only one for which even a small amount of high-level (typically 240 mb or 11–12 km) flight-track data were available. Their results may be suspect, however, because of problems with the navigation systems used. Future Doppler-radar flights can perhaps determine whether the sloping tangential wind maximum seen in Alicia is characteristic only of less intense storms, as suggested by Shea and Gray, or is a more general trait of hurricanes.

The most prominent features of the radial wind in Alicia (Fig. 8) were inflow into the eyewall in the lower troposphere (strongest at heights of 2.0–4.5 km) and a concentrated layer of intense radial outflow (8–9 m s^{-1}) from the eyewall at 10–14 km height. These features are also consistent with the numerical modeling

results of Willoughby et al. (1984a, their Fig. 8) and the flight-track data composites of Shea and Gray (1973), Willoughby et al. (1983), and Jorgensen (1984b). However, the limited amount of jet aircraft data included in Shea and Gray's study did not yield radial wind information at upper levels and, as noted above, the other studies were confined to the lower troposphere. Hence, the Doppler radar data in Fig. 8 provide the first observational confirmation of the radial outflow layer concentrated at upper levels in the hurricane inner core by aircraft.

The radial wind field seen in Fig. 8 exhibited an asymmetry in the low-level inflow not evident in Jorgensen's (1984b) study of Hurricane Allen. In box 1, it extended outward from the eyewall only to 18 km from the storm center where radial outflow extended through the 1.5–5.0 km layer, while in box 2, radial inflow was present inside 40 km up to 3.3 km altitude. This structure is, however, consistent with observations of asymmetry in other hurricanes. Willoughby et al. (1984b) noted that in tropical cyclones embedded in an environmental current characterized by westerly shear the west sides of hurricanes frequently are characterized by outflow at low levels (1500 m).

5. Inner-core dynamics implied by observed structure

In this section, we summarize the storm circulation that can be inferred from the foregoing airborne Doppler radar analyses and compare it to other recent work on hurricane inner-core dynamics. Figure 9 is a schematic summary gleaned from Figs. 3–8. The Appendix explains in more detail how the diagram was constructed. The vertical cross section (Fig. 9a) resembles the schematic model of Jorgensen (1984b; see his Fig. 19) and may be regarded as a confirmation, refinement and extension of his work. The following subsections describe the important components of the inner-core air motions indicated in Fig. 9a. The precipitation trajectories in Fig. 9a, b will be discussed in section 6.

a. Secondary circulation

Ooyama (1982) has pointed out that the essential ingredients of a fully developed hurricane eyewall circulation are a primary (azimuthal) circulation extending throughout the depth of the troposphere and a secondary (radial-vertical) circulation consisting of "persistent updraft and precipitation in the eyewall clouds, the inward spiraling airflow in a relatively thin layer above the ocean surface, and the radial outflow in an upper layer of the vortex." He contends that the secondary circulation is essential to the formation and maintenance of the primary circulation and of the tropical cyclone as a whole.

In Fig. 9a the primary circulation is indicated by the dashed isotachs. The Doppler radar data also show the secondary circulation clearly (wide, hatched, streamlines), except where it is disrupted by convective

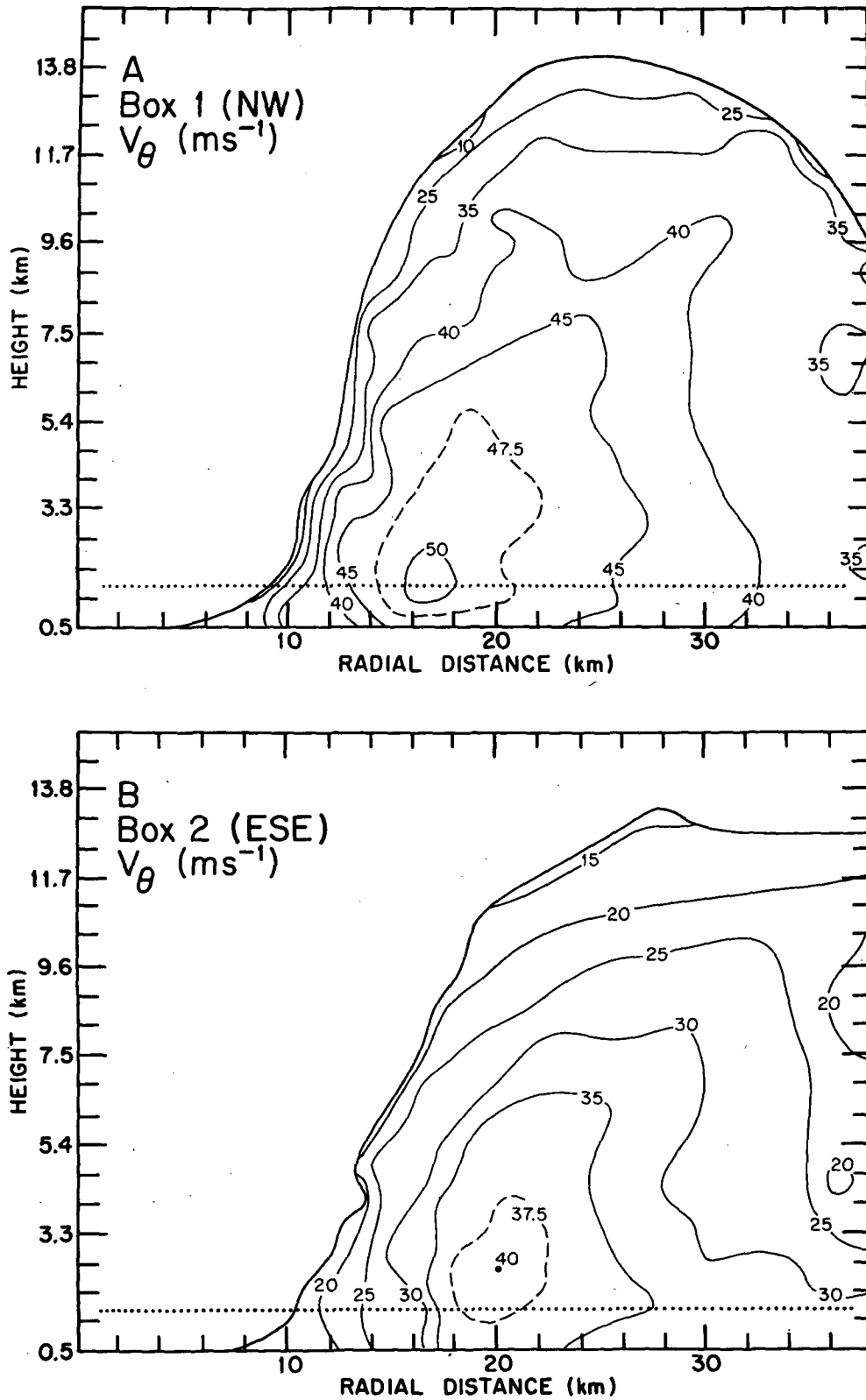


FIG. 7. Radius-height analyses of the azimuthally averaged tangential wind speed (V_{θ} , m s^{-1}) for (a) box 1 and (b) box 2. The solid line delineates the boundary of the analysis region [the 5 dB(Z) contour].

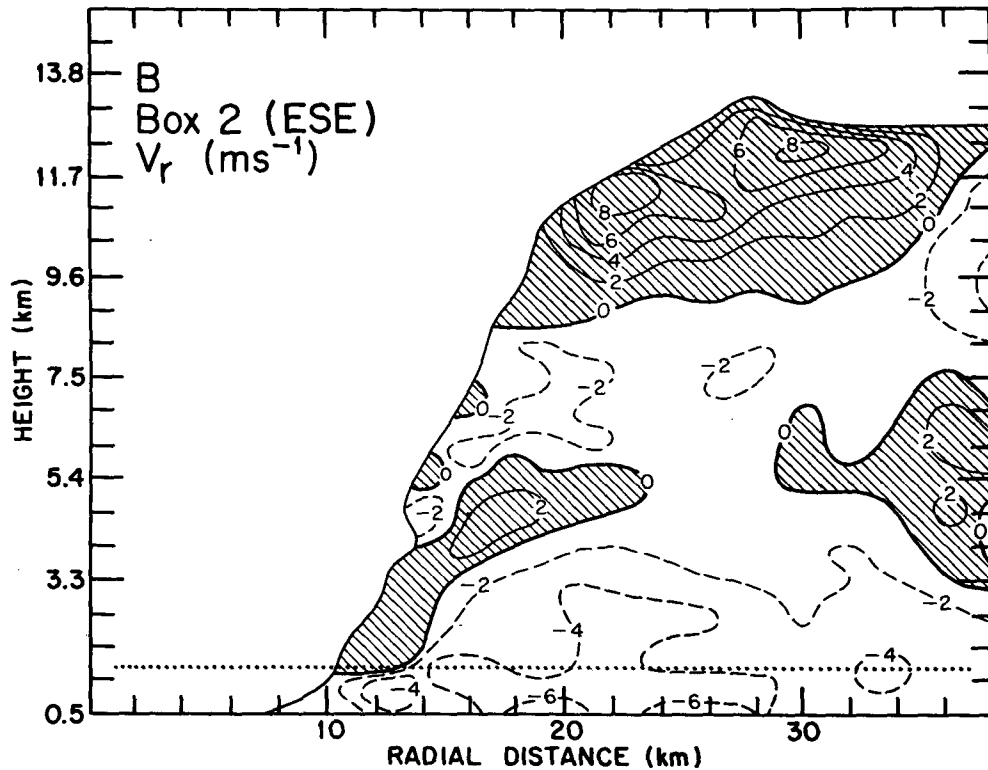
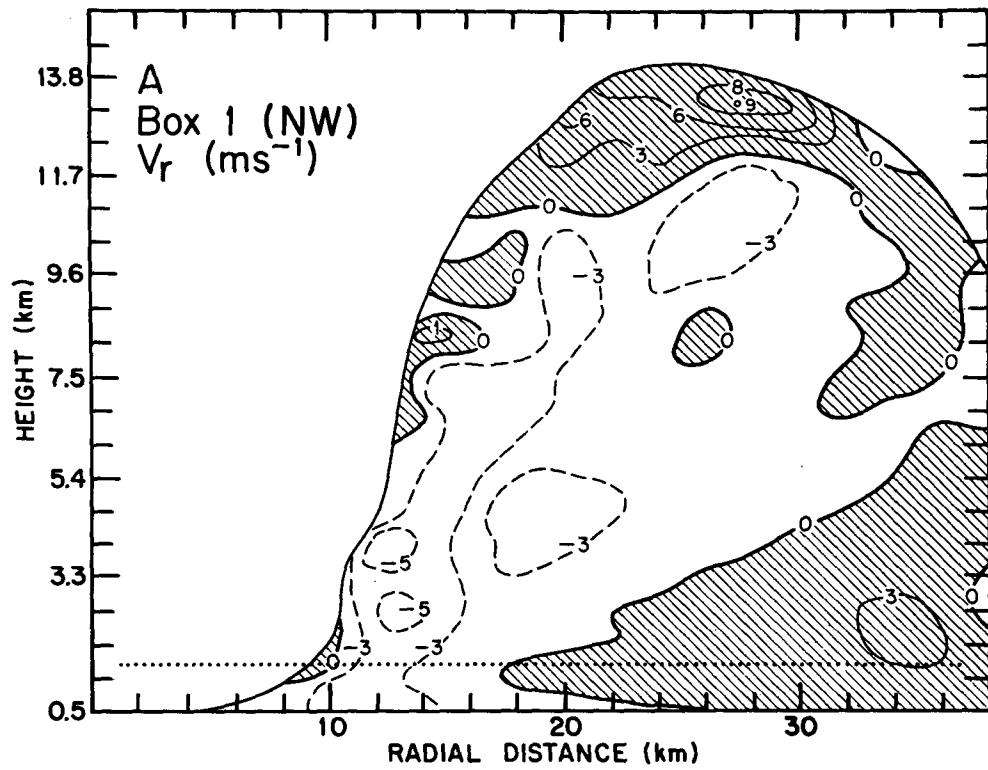
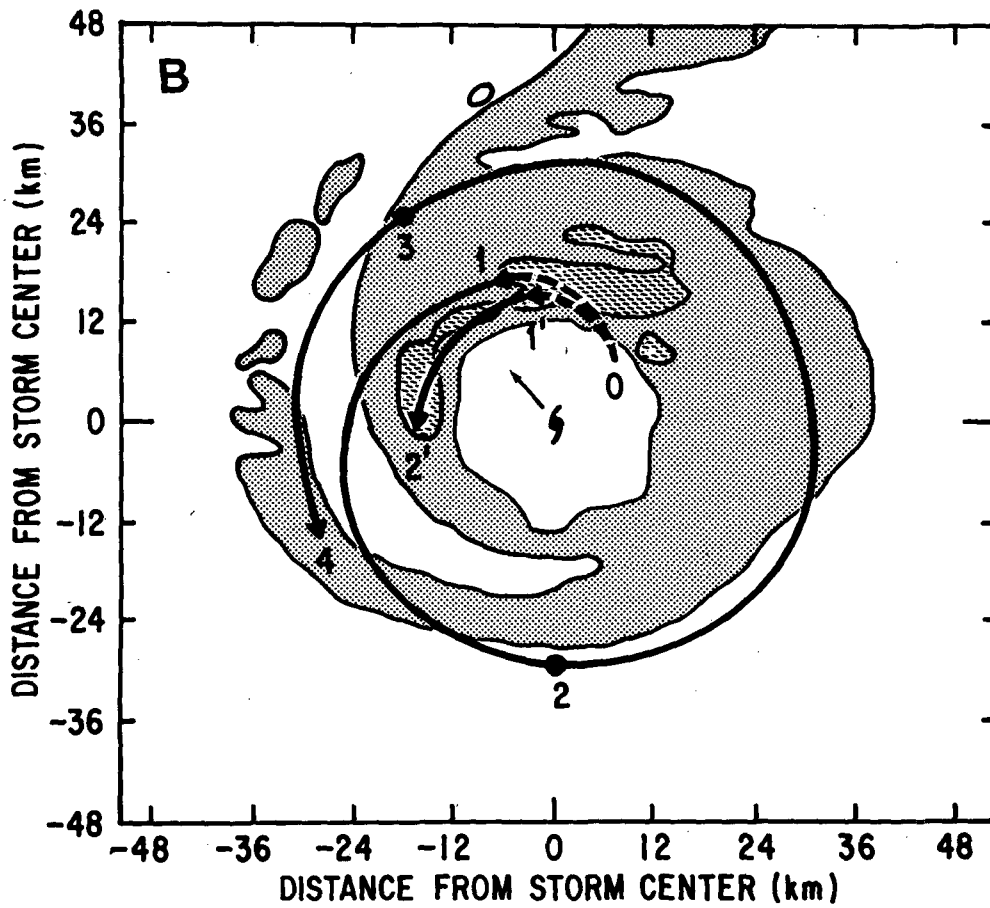
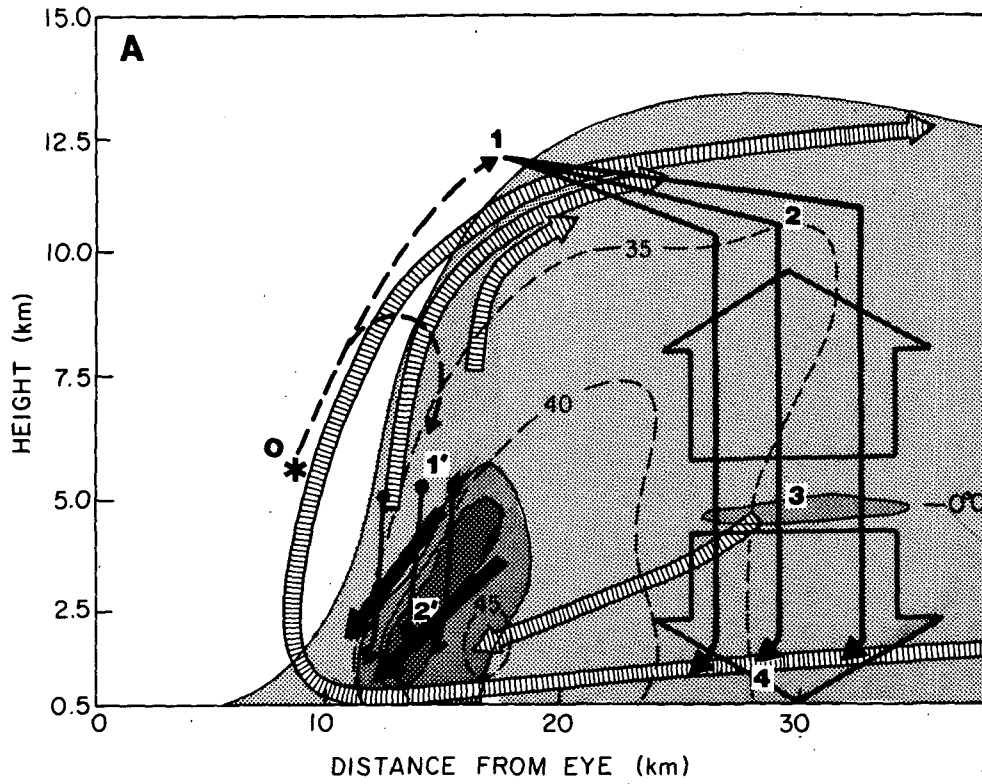


FIG. 8. Radius-height analyses of the azimuthally averaged radial wind speed (V_r , m s^{-1}) for (a) box 1 and (b) box 2. Solid contours are positive and dashed contours negative. Positive values (outflow) are shaded. The solid line delineates the boundary of the analysis region [the 5 dB(Z) contour].



downdrafts in the region of heavy eyewall rainfall (wide, black streamlines). The Doppler observed secondary circulation resembles those derived theoretically by Shapiro and Willoughby (1982), especially with respect to the radially outward sloping ascending branch of the circulation. They found that similar structures were formed by a heat (or momentum) source near the radius of maximum wind in a hurricane-like primary vortex.

As pointed out in section 1, composites of flight-track wind data have shown certain features of the secondary circulation in hurricanes below 6 km. The Doppler radar data now, for the first time, provide observations of the whole secondary circulation, including its upper-level portion, in a single storm. The data support the studies of Shapiro and Willoughby (1982) and Willoughby et al. (1984) and the upper-level part of the schematic model hypothesized by Jorgensen (1984b) from midtropospheric, flight-level data.

b. Convective updrafts and downdrafts

Ooyama (1982) argued that convectively unstable motions must be superimposed on the upward branch of the secondary circulation. Positive buoyancy is required to produce entrainment of inward flowing air above the boundary layer. In Fig. 8, we saw that radial flow toward the eyewall existed through a deep lower tropospheric layer with maximum inflow at 2.0–4.5 km. Ooyama points out that in addition to the secondary circulation, inflow into the eyewall must occur above the boundary layer in order for the hurricane to intensify. This air must be entrained into the upward branch of the secondary circulation and transported up to outflow levels to maintain the primary circulation. Evidence that small-scale convective updrafts were indeed superimposed on the secondary circulation, depicted in Fig. 9a, is clearly seen in the vertical-incidence Doppler data (Fig. 6). The rising branch of the secondary circulation contained discrete bubbles of concentrated rising motion. Convective cloud forms seen along the inside edge of the eyewall (e.g., Fig. 20 in Jorgensen, 1984b) are a further indication of cellular structure superimposed on the secondary circulation.

The magnitudes of the updraft maxima seen in Fig. 6 are consistent with those reported by Jorgensen et al. (1985). Their data were obtained along flight tracks located at altitudes less than 6 km. At these levels, the Doppler data in Fig. 6 show peak updraft magnitudes

of 3–6 m s^{-1} , which are similar to the values of the strongest 10% of the updrafts discussed by Jorgensen et al. (1985).

Our results provide the first observational indication of the magnitudes of the updraft peaks at altitudes above 6 km. The model results of Lord et al. (1984) suggest that peak updraft intensities should be found at heights of 6–14 km. The Doppler data in Fig. 6, as well as in vertical cross sections obtained at times other than those shown, indicate that the most intense updraft peaks were indeed at these levels in Alicia.

Convective downdrafts were also superimposed on the secondary circulation. As indicated by the vertical incidence Doppler radar data in Fig. 6 and by the schematic diagram (Fig. 9a), convective-scale downdrafts dominated the region of high radar reflectivity at low levels underneath the sloping updraft. The location of convective downdrafts throughout the region of maximum reflectivity was suggested by Jorgensen (1984b) in his schematic model (Fig. 19 of his paper) but was not clearly shown by the data available to him except in the form of a statistical correlation of flight-level downdraft velocity and reflectivity. The location of the downdraft motion throughout the region of maximum reflectivity is indicative of precipitation drag playing a role in the downdraft generation. Evaporation as a result of entrainment of dry air from the eye of the storm into the precipitation core could also have been involved in the downdraft dynamics.

Although the downdraft motions interrupt the flow of the secondary circulation at low levels in the vicinity of the eyewall rain maximum, the peak downdraft velocities were rather weak, typically 2–3 m s^{-1} . These downdrafts probably did not have a strong feedback to the larger circulation. Ooyama (1982) and Willoughby et al. (1984a) suggest that in the mature eyewall, the upward motion is associated more with the frictional convergence of the inwardly spiraling low-level branch of the secondary circulation than with downdraft-induced convergence.

c. Mesoscale up- and downdrafts

The large block arrows in Fig. 9a indicate the locations of the mesoscale up- and downdrafts described in section 4. These drafts resemble those observed in tropical squall lines both in magnitude (\sim tens of centimeter per second on average) and in that they emanate from near the 0°C level (Leary and Houze, 1979;

FIG. 9. (a) Schematic of the radius–height circulation of the inner core of Hurricane Alicia. Shading depicts the reflectivity field, with contours at 5, 30 and 35 dBZ. The primary circulation (V_θ , m s^{-1}) is depicted by dashed lines and the secondary circulation by the wide hatched streamlines. The convective downdrafts are denoted by the thick solid arrows, while the mesoscale up- and downdrafts are shown by the broad arrows. The level of the 0°C isotherm is labeled. (b) A schematic plan view of the low-level reflectivity field in the inner core of Hurricane Alicia superimposed with the middle of the three hydrometeor trajectories shown in (a). The reflectivity contours in (b) are 20 and 35 dBZ. Note that the storm center and direction are also shown. In (a) and (b) the hydrometeor trajectories are denoted by dashed and solid lines labelled 0–1–2–3–4 and 0–1'–2'. (See the Appendix for the details of the construction of the circulation schematic for the precipitation trajectories).

Gamache and Houze, 1982; Houze and Rappaport, 1984). Lord et al. (1984) have indicated by model calculations that the mesoscale downdraft in a hurricane is probably initiated by the melting of hydrometeors. [This mechanism was suggested for tropical squall lines by Leary and Houze (1979)]. Our results provide the first direct observational evidence that the top of the mesoscale downdraft in a hurricane is located near the melting level.

d. Asymmetric structure

The asymmetric character of the hurricane circulation has been noted by a number of authors (e.g., Black and Anthes, 1971; Shea and Gray, 1973; Frank, 1977; Frank, 1984). It appears to be related to the movement of the storm through its environment and over the earth's surface.

Shapiro's (1983) theoretical study of the effects of storm motion on the boundary-layer flow of a hurricane over open ocean found that the storm motion produces enhanced convergence in the boundary layer, in the front of the traveling storm. In his example of a slow-moving storm (velocity $< 5 \text{ m s}^{-1}$), the maximum horizontal winds, convergence, and the peak vertical velocity at the top of the boundary layer occurred within the eyewall region ahead of the storm.

Willoughby et al. (1984b) described the asymmetric nature of the hurricane circulation above the boundary layer, in which there is a mean transport of air across the vortex, induced by the motion of the storm through a vertically sheared environment. They found that for a hurricane moving with the wind at an intermediate steering level in an environment that has westerly shear (i.e., the relative environmental flow is easterly at low levels and westerly aloft), there is an east-west flow across the vortex at low levels and an eastward streaming of the cirrus clouds in the outflow layer near the tropopause.

The observed asymmetries in the circulation of Hurricane Alicia, as shown in Figs. 6–8, are consistent with the results of both Shapiro (1983) and Willoughby et al. (1984b). As found by Shapiro (1983), the eyewall updrafts in the front of the storm (legs 1 and 2, Fig. 6a–b) are much stronger than those behind the storm (leg 3, Fig. 6c). The Doppler observations indicate, moreover, that this is not only true at the top of the boundary layer, as discussed by Shapiro, but also throughout the depth of the eyewall.

This front-back asymmetry in the eyewall updraft apparently resulted in a front-back asymmetry in the altitude of the outflow layer. The altitude of the outflow layer at the top of the eyewall, as depicted in Fig. 8, was lower on the east side of the storm where the vertical velocities throughout the depth of the eyewall were the weakest. The altitude of the outflow layer on the west side of the storm was higher by 1.5–2.0 km.

The Doppler analysis also showed an east-west asymmetry in the inflow layer (altitudes from 1.5–5.0 km) outside of the eyewall, similar to that described

by Willoughby et al. (1984b). The radial flow in Fig. 8 shows inward radial motion on the east side of the storm outside the eyewall (box 2, Fig. 8b) and outward radial motion on the west side (box 1, Fig. 8a). These Doppler observations are consistent with an analysis of the 1.5 km flight-level winds in Alicia (Willoughby, personal communication).

6. Precipitation trajectories

As discussed by Houghton (1968) and Houze (1981), precipitation mechanisms in clouds can be divided into convective processes in which particles form at low levels and are carried upward by strong drafts until they grow to sufficient size to fall out, and stratiform processes in which vertical air motions are weak and precipitation particles drift down from the upper reaches of the cloud toward the earth's surface while they grow. Houze (1981) pointed out that most precipitating cloud systems contain both convective and stratiform processes, typically working in concert. Hurricanes are no exception. In the inner core, the ascending branch of the secondary circulation, with its superimposed small-scale updraft cores, provided an environment conducive to the convective precipitation formation. The magnitude of the upward velocity ($6\text{--}10 \text{ m s}^{-1}$) was great enough to carry hydrometeors initiated at low to mid-levels upward (dashed particle trajectories in Fig. 9a). When these particles fell out below the sloping updraft (see solid particle trajectories 12–15 km from the eye in Fig. 9a), they evidently produce the convective downdraft (wide, heavy streamlines) through precipitation drag and possibly through evaporative cooling as well. Ice particles reaching the outflow layer of the secondary circulation (e.g., along path 0–1 in Fig. 9a) were advected outward into the stratiform region. Once in the stratiform region, they fell slowly. They continued to be advected horizontally until they reached the base of the outflow layer (25–35 km from the eye). Then they fell almost vertically through the mesoscale updraft, where they undoubtedly continued to grow by acquisition of excess vapor generated by the mesoscale ascent (further discussion in section 7). The particles probably also underwent considerable aggregation above the melting level at which level they produced the bright band. While the particles continued to fall as raindrops below the melting level, they may have undergone evaporation if they encountered unsaturated air.

The horizontal projections of the middle two trajectories in Fig. 9a are shown in Fig. 9b. The basis for these trajectories is given in the Appendix. The trajectory labelled 0–1'–2' is the path of the precipitation particle that fell to the surface in the eyewall convective rainband. The trajectory labelled 0–1–2–3–4 represents the path of the particle that fell in the surrounding region of stratiform precipitation. As the particle in the eyewall fell from 1'–2', it traversed a horizontal path down the center of the eyewall rainband 18–20 km, or one quarter of the way around the storm. The particle

following this trajectory required ~ 10 min to reach the ground. This path is consistent with the upwind-sloping precipitation cores seen in the eyewalls of other hurricanes (e.g., Marks, 1985). The precipitation particle carried by the upper-level outflow into the stratiform region surrounding the eyewall made more than one complete circuit around the storm before it reached the surface in the "connecting band" (cf. Fig. 1b). The path 1-2-3-4 took 1-2 h.

These long horizontal paths emphasize the importance of the strong tangential winds in distributing precipitation in a hurricane. Precipitation is swirled around the storm, and particles at a given point in the stratiform region surrounding the eyewall typically will have come from a variety of locations within the eyewall. The occasional observation of stratiform rainbands outside the eyewall region of a hurricane far from any active convection (e.g., the connecting band or bands) may be explained by the arrival of particles from a distant location upwind.

7. Water budget and inner-core region

The water budget of the hurricane inner-core region was examined by subdividing it into the eyewall (or convective) region, dominated by the upward branch

of the secondary circulation, and the stratiform region, where the mesoscale updraft and downdrafts prevailed (Fig. 10). A similar partitioning of the water budget into convective and stratiform regions has been applied to both tropical squall lines and nonsquall cloud clusters (Houze, 1977; Gamache and Houze, 1983; Churchill and Houze, 1984; Houze and Rappaport, 1984; Leary, 1984). These studies showed that in nonhurricane mesoscale systems, typically 30-50% of the total precipitation falls as stratiform rain. Marks (1985) found that in Hurricane Allen, 60% of the total precipitation of the inner-core region (within a radius of 110 km) fell in the stratiform region (referred to by him as the "rainband" zone). Using the same criterion to partition the precipitation as that in Marks (1985), the results for this period in Alicia indicate that 62% of the total precipitation within a radius of 40 km fell in the stratiform region surrounding the eyewall. The predominance of stratiform precipitation, if typical, requires understanding and explanation.

To investigate the source of the stratiform condensate, we have adopted the notation of Gamache and Houze (1983). In Fig. 10, the terms C_{mu} and C_A are sources of condensate in the stratiform region; C_{mu} represents water condensed in the mesoscale updrafts, while C_A represents hydrometeor mass condensed in

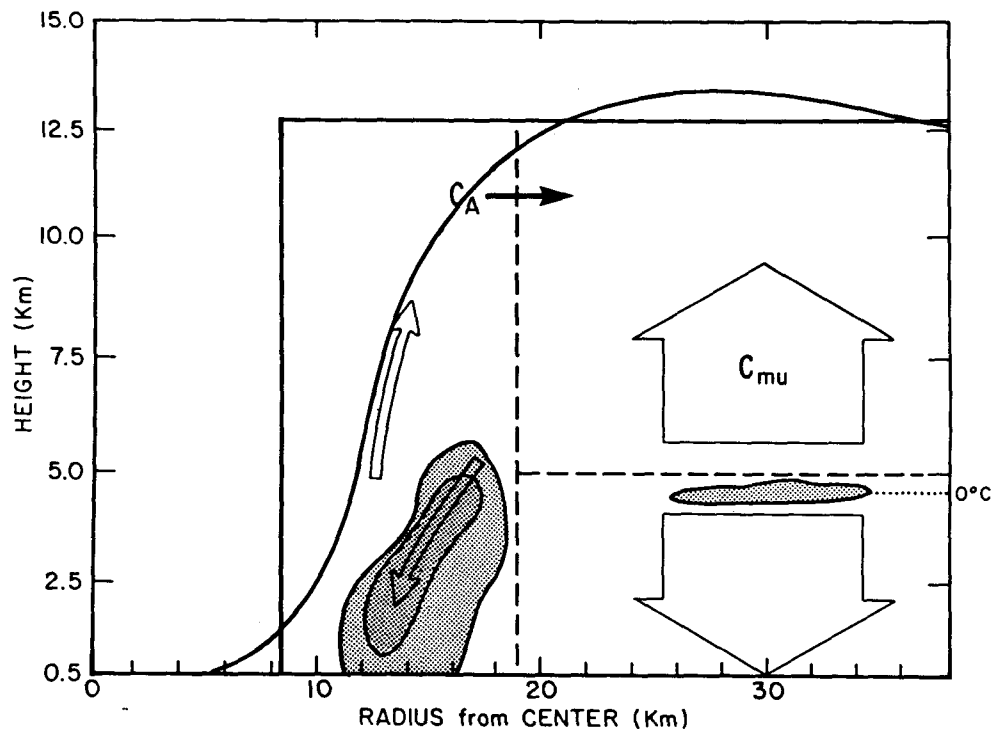


FIG. 10. Schematic of the radius-height structure of the inner core of Hurricane Alicia depending the portions of the storm discussed in the water budget computations. Shading depicts the reflectivity field, with contours at 5, 30, and 35 dBZ. The boxes superimposed over the reflectivity delineate the convective region from the stratiform region, and the mesoscale upward motion from the mesoscale downward motion in the stratiform region. In the convective region the arrows denote the convective up- and downdrafts. The mesoscale up- and downdrafts are shown by the broad arrows and the level of the 0°C isotherm is labeled. (See text for definition of the water budget terms.)

updrafts in the convective region and subsequently transported into the stratiform region. Gamache and Houze (1983) found that $C_{mu} \approx 0.35C_A$ for a tropical squall line; i.e., convectively generated condensate appeared to be a somewhat larger source of condensate for the stratiform region than was water condensed in situ. They computed C_{mu} by inferring the mean vertical velocity in the mesoscale updraft from divergence calculated from composite rawinsonde data, while C_A was determined as a residual of other terms in the water budget. However, this calculation involves many assumptions and uncertainties, so that one can only conclude that both C_{mu} and C_A contribute substantially to the mass of the stratiform cloud in the squall line case. In the present study, the Doppler data allow us to calculate C_{mu} and C_A more directly for Hurricane Alicia, thereby obviating some assumptions of Gamache and Houze.

To estimate C_{mu} we assume the mean vertical velocity in the mesoscale updraft to be $\bar{w} = 0.4 \text{ m s}^{-1}$, the approximate value determined from the vertical-incidence Doppler data in Fig. 6a. The air density is assumed to be 0.4 kg m^{-3} (corresponding to the density at an altitude of 10.5 km using the density relationship described in section 3) in the mesoscale updraft, and the water vapor mixing ratio is assumed to be 0.0063 at the base of the updraft (corresponding to 85% relative humidity at 540 mb) and 0.0003 at the base of the outflow level (corresponding to 75% relative humidity at 250 mb). The stratiform region is assumed to cover an annular area of $3.64 \times 10^9 \text{ m}^2$ located between 21 and 40 km from the eye of the storm. The condensation rate in the mesoscale updraft is thus estimated to be $(0.4 \text{ m s}^{-1})(0.4 \text{ kg m}^{-3})(3.64 \times 10^9 \text{ m}^2)(0.0063 - 0.0003) = 3.49 \times 10^6 \text{ kg s}^{-1} = C_{mu}/\tau$, where τ is the time period during which the mass of water C_{mu} is condensed.

To estimate C_A , we refer to the radial velocity shown in Fig. 8. From this figure, we infer that the radial outflow at a distance of 21 km from the eye of the storm (the outer edge of the eyewall) occurs primarily in a layer 3000 m deep (between 10 and 13 km) and has a typical speed $\bar{V}_r = 6 \text{ m s}^{-1}$. The difference in hydrometeor mixing ratios across the outer edge of the eyewall in this layer is assumed to be 0.5 g m^{-3} . This value is based on the model simulation of Lord et al. (1984; see their Figs. 5 and 6) which showed regions of snow mixing ratio $> 0.8 \text{ g m}^{-3}$ surrounded by areas $\leq 0.4 \text{ g m}^{-3}$. The flux of condensate across the boundary between the convective (eyewall) and stratiform regions is then estimated to be $(6 \text{ m s}^{-1})(0.5 \text{ g m}^{-3})(3000 \text{ m})(2\pi)(21 \times 10^3 \text{ m}) = 1.19 \times 10^6 \text{ kg s}^{-1} = C_A/\tau$.

Thus, the Doppler data suggest that $C_{mu} \approx 2.94 C_A$. The in situ production of condensate appears to have dominated—just opposite from the squall line case, in which Gamache and Houze (1983) found C_{mu} and C_A to both be important, but with C_A dominating. It should be noted that these results are sensitive to the size of the area encompassing the mesoscale updraft and the

depth and altitude of the outflow layer. As pointed out in Sec. 5, these features may be asymmetrically arranged around the storm, thus altering our results.

Although these results must be regarded cautiously at this juncture, it is tempting to conclude that in the case of the hurricane, the mesoscale updraft has a stronger effect on the growth of hydrometeors than in the squall line because it is associated with the secondary circulation driven by vortex-scale dynamics. The squall line is not embedded in any equivalent dynamic feature.

8. Conclusions

On 17–18 August 1983, Hurricane Alicia was moving northwestward toward the Texas coast. Continuous quantitative ground-based radar observations from the National Weather Service WSR-57 radar at Galveston, Texas, showed a closed eyewall surrounded by outer rainbands. At 0108–0200 UTC on 18 August, an intense outer band was just reaching the coastline, while the eyewall was still over water. During this time, the NOAA WP-3D aircraft equipped with Doppler radar flew radial passes across the eyewall making Doppler measurements in two quadrants of the storm. An analysis of the three-dimensional wind field in the eyewall region was derived from the airborne Doppler data. The vertical velocity was derived from vertical incidence Doppler data and reflectivity collected along three legs of the flight track, and the horizontal components of the wind were derived in two regions of the storm by pseudo-dual-Doppler synthesis of the wind components along the radar beam for two pairs of flight legs. Because of the time elapsed between flight legs used in the dual-Doppler synthesis (47–52 min), only the azimuthally averaged tangential and radial components of the circulation could be resolved for each analysis region. However, this information combined with the vertical incidence data nonetheless provided an unprecedented comprehensive view of the primary, secondary and superimposed convective circulation features in a single storm.

The following specific results were obtained:

- 1) The primary (azimuthal) circulation was characterized by a core of maximum tangential wind that sloped radially outward with height. The Doppler radar data for this single case thus confirms the slope of the tangential wind maximum seen both in composites of flight-level data (Willoughby et al., 1982; Jorgensen (1984a,b) and in model simulations (Willoughby et al., 1984a). Peak winds were at low levels (1.5–2.5 km) and on the northwest (leading side) of the storm.

- 2) The secondary (radial-height) circulation was characterized by a lower tropospheric layer of inward directed flow that extended well above the boundary layer, with maximum inflow at 2.0–4.5 km altitude, and a layer of intense radial outflow from the eyewall concentrated at upper levels (10–14 km). The rising

branch of the secondary circulation in the eyewall region sloped out from the center in agreement with theoretical studies (Shapiro and Willoughby, 1982). The airborne Doppler radar data provide observational confirmation of the upper tropospheric portion of the secondary circulation predicted by numerical model simulations (Willoughby et al., 1984a) but which could not be shown by previous flight-level datasets.

3) Convective-scale updrafts and downdrafts were superimposed on the secondary circulation in the eyewall region in a pattern which confirms theoretical arguments given by Ooyama (1982). Discrete cores or bubbles of more intense upward motion were located along the axis of the outwardly sloping rising branch of the secondary circulation. These updraft cores appeared to become stronger above 6 km altitude (the height of the 0°C isotherm in the eyewall). In the region of concentrated heavy rains at low levels in the eyewall, the secondary circulation was interrupted by convective downdrafts, which coincided with vertical cores of high reflectivity and spread out at low levels. Prior to this study, these convective downdrafts have not been convincingly shown because of the difficulties of obtaining flight-level data at low altitudes.

4) The stratiform precipitation region located just outside the eyewall appeared to be characterized by general ascent (averaging 0.3–1.3 m s⁻¹) above the melting layer and descent of slightly smaller magnitude below. Uncertainty in estimating the fall velocities of rain make the inference of the downdraft somewhat uncertain. However, the mesoscale updraft above the melting layer and downdraft are also seen in tropical squall lines and other mesoscale convective systems. The ascent aloft in this case was apparently part of the secondary circulation associated with condensational heating in the eyewall region (Shapiro and Willoughby, 1982), while the descent below was probably driven by melting (Lord et al., 1984). The Doppler radar data provide the first direct observational confirmation of descent occurring at and below the melting level in a hurricane.

5) The Doppler-derived wind field analyses enabled the construction of hydrometeor trajectories in the inner core of the storm. Particles that formed in the upward branch of the secondary circulation evidently followed two basic paths: 1) large hydrometeors, with fall-speeds greater than updraft velocity, fell out of the updraft and formed the eyewall reflectivity maximum; 2) smaller hydrometeors, with fall-speeds less than the updraft velocity, were swept up to the outflow layer at the top of the eyewall and carried outward, where they seeded the region containing the mesoscale updraft. The particles falling in the eyewall reached the sea surface within 10 min and traveled 18–20 km downwind, consistent with the upwind slope with increasing altitude of reflectivity cores in the eyewall. The hydrometeors that seeded the mesoscale updraft region fell so slowly before they reached the melting level that they took 1–2 h to reach the surface. These trajectories

suggest that the precipitation falling at any location in the stratiform region typically contained particles arriving from a variety of locations in the eyewall after they had circulated as many as 1½ times around the storm.

6) The Doppler radar data allow the hurricane water budget to be examined quantitatively for the first time. Calculations based on the Doppler wind synthesis suggest that, while the eyewall outflow layer was a major source of hydrometeors to seed the stratiform region, condensation owing to mesoscale ascent within the stratiform region itself provided an environment conducive to vigorous growth of hydrometeors. The mass of water condensed by the mesoscale lifting exceeded that transported into the stratiform region in the upper-level eyewall outflow by a factor of 3.

The results of this study clearly demonstrate the usefulness of airborne Doppler radar for determining the detailed circulation patterns in a hurricane. With this remote-sensing technique we have been able to carry observational work on hurricanes farther than has been possible with flight-level data. Many features of inner-core storm structure have now been observed in a single case, and features that have been difficult or impossible to infer from traditional in situ data have been observed successfully. Theoretical results have been confirmed, and the three-dimensional Doppler-derived wind field combined with the observed reflectivity field has allowed the beginnings of quantitative studies of precipitation growth patterns and the storm water budget.

In the future, we intend to improve the airborne Doppler reconstruction of the storm air motions by reducing the time between flight legs so that w may be computed by mass continuity and thus obtained over a larger volume of the storm. We also hope to sample the inner core of mature storm more intensively by using more than one aircraft equipped with Doppler radar. In this way, we expect to achieve a still greater understanding of the precipitation mechanisms, dynamics, and water budget of a mature hurricane.

Acknowledgments. The data used in this study were gathered with the aid of the NOAA Office of Aircraft Operations flight crews and engineers. Their skill and dedication is greatly appreciated. David Jorgensen helped design the Doppler analysis software and provided many helpful suggestions during the derivation of the Doppler wind analysis. We appreciate helpful discussions with Peter Black, Robert Black, Robert Burpee, Stephen Lord, Mark Powell, Lloyd Shapiro, Paul Willis, and Hugh Willoughby. This research was partially supported by the National Science Foundation under Grant ATM 84-13546.

APPENDIX

Construction of Schematic Diagram

The schematic representation of the inner-core structure presented in Fig. 9 was based objectively on the airborne radar observations. The following discus-

sion indicates how each of the items in the figure were derived from the data.

a. Radar reflectivity

The reflectivity field was constructed by averaging the reflectivity fields observed on legs 1 and 2 of the flight track. These legs represent the region of the eyewall that contained the most intense reflectivity.

b. Air motions

The primary (tangential) circulation shown in Fig. 9a is the average of the V_θ fields in boxes 1 and 2. The secondary circulation, shown by the wide hatched arrows in Fig. 9a, as well as the convective downdrafts, shown by wide black arrows, were obtained by fitting streamlines to mean motion vectors in a radial-height plane (Fig. A1). The vectors were obtained by addition of the mean vertical velocity field from legs 1 and 2 and the mean radial wind field from boxes 1 and 2. Both w and V_θ fields were computed on a grid 3×1.5 km in the radial and vertical direction, respectively. Streamlines drawn to fit the vectors in Fig. A1 were transferred directly to Fig. 9a. The large black arrows in Fig. 9a were drawn to indicate a mesoscale updraft above and downdraft below the melting layer. These mean vertical motions, computed from the Doppler radar data collected on legs 1 and 2, were discussed in section 4a.

c. Particle trajectories

Hypothetical precipitation particle trajectories were constructed using the radius-height airflow shown in Fig. 9a and particle fallspeeds consistent with those in Fig. 5.

The upward hydrometeor trajectory labeled 0-1 in Fig. 9 was computed assuming a particle ascent rate ($w + V_i$) of 5 m s^{-1} from an altitude of 6-12 km. This ascent rate is in good agreement with Figs. 5 and 6. The horizontal displacement of this trajectory in Fig. 9b was computed using a V_θ of 10 m s^{-1} and a V_r of $1-2 \text{ m s}^{-1}$ throughout the altitude range 6-12 km. For the upward trajectory labeled 0-1' in Fig. 9, V_θ and V_r were identical to that of trajectory 0-1, but this particle was assumed to have grown more vigorously during its ascent so that it quickly fell out of the updraft.

The middle convective downdraft trajectory labeled 1'-2' in Fig. 9 was calculated assuming that $w + V_i = -7 \text{ m s}^{-1}$ in the altitude interval from 5.5 km to the surface, again in good agreement with Figs. 5 and 6. The horizontal displacement of trajectory 1'-2' in Fig. 9b was derived using V_θ of 40 m s^{-1} and a V_r of -3 m s^{-1} in this altitude interval. These values are consistent with Figs. 7 and 8.

The outflow-layer particle trajectories labeled 1-2-3-4 in Fig. 9 were determined using a range of V_r , V_θ , and $w + V_i$ values consistent with Figs. 5-8. The three trajectories represent those of particles with initial $w + V_i$ values at point 1 of -0.5 (rightmost), -0.75 (cen-

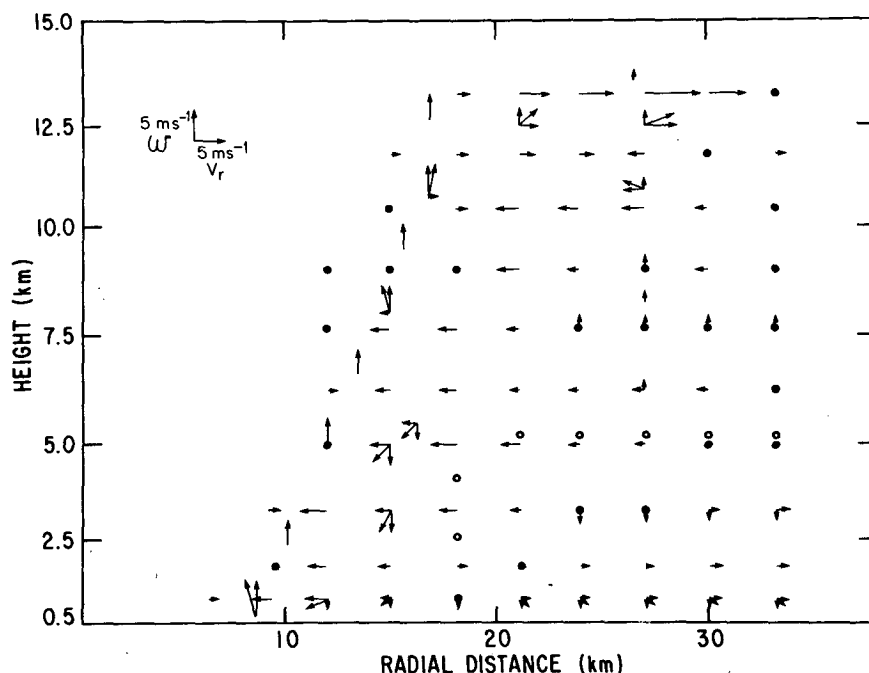


FIG. A1. Radius-height cross section of the V_r and w fields used to construct Fig. 9a. Arrows indicate the magnitude and orientation of the V_r and w values. Solid circles denote zero radial velocity and open circles denote zero vertical velocity (see text for details). The V_r and w pairs are drawn at a number of locations to indicate the resultant vectors used in the construction of Fig. 9a.

ter), and -1.5 m s^{-1} (leftmost), respectively. From 1–2 the particles are within the outflow layer at altitudes of 10–12 km, with $V_r = 4.5 \text{ m s}^{-1}$ and V_θ having a range of values: 1) from 18–21 km radius, $V_\theta = 20 \text{ m s}^{-1}$; 2) from 21–24 km radius, $V_\theta = 23 \text{ m s}^{-1}$; 3) from 24–27 km radius, $V_\theta = 27 \text{ m s}^{-1}$; and 4) from 27–30 km radius, $V_\theta = 35 \text{ m s}^{-1}$. As shown in Fig. 9a, b, at point 2 the hydrometeors reach a radial distance of 25–35 km from the center and travel almost half way around the storm. At this point they have fallen out of the outflow layer.

From 2–3, the hydrometeors were falling through the mesoscale updraft (5–10 km in altitude). In this layer, we have assumed $w + V_r$ has doubled due to particle growth. In this region $V_\theta = 35 \text{ m s}^{-1}$ and V_r was essentially zero. The possible particle trajectories diverge greatly in this region. Slightly increased particle growth by aggregation or riming could have caused some hydrometeors to fall even faster than we have hypothesized. Also small asymmetries in the radial wind direction and the mesoscale updraft strength would have resulted in different horizontal trajectories. Trajectory 2–3 is considered to be a good approximation to the trajectories of typical particles in this region.

After these particles melted they followed trajectory 3–4 (5 km to surface in altitude) where $w + V_r$ decreases dramatically to -5 m s^{-1} (consistent with Fig. 5). The V_θ stays near 35 m s^{-1} and V_r is near zero until the lowest layers where the particles entered the inflow layer.

The horizontal displacement of the particles in trajectory 1–2–3–4, as depicted in Fig. 9b, show that these particles completed 1–1.5 circuits around the storm during the 1–2 h it takes a particle to fall from the outflow layer.

REFERENCES

- Atlas, D., R. C. Srivastava and R. S. Sekhon, 1973: Doppler radar characteristics of precipitation at vertical incidence. *Rev. Geophys. Space Phys.*, **11**, 1–35.
- Beard, K. V., 1985: Simple altitude adjustments to raindrop velocities for Doppler radar analysis. *J. Atmos. Ocean. Tech.*, **2**, 468–471.
- Black, P. G., and R. A. Anthes, 1971: On the asymmetric structure of the tropical cyclone outflow layer. *J. Atmos. Sci.*, **28**, 1348–1366.
- Case, R. A., and H. P. Gerrish, 1984: Atlantic hurricane season of 1983. *Mon. Wea. Rev.*, **112**, 1083–1092.
- Churchill, D. D., and R. A. Houze, Jr., 1984: Mesoscale updraft magnitude and cloud-ice content deduced from the ice budget of a tropical cloud cluster. *J. Atmos. Sci.*, **41**, 1717–1725.
- Frank, W. M. 1977: The structure and energetics of the tropical cyclone. I. Storm structure. *Mon. Wea. Rev.*, **105**, 1119–1135.
- , 1984: A composite analysis of the core of a mature hurricane. *Mon. Wea. Rev.*, **112**, 2401–2420.
- Gamache, J. F., and R. A. Houze, Jr., 1982: Mesoscale air motions associated with a tropical squall line. *Mon. Wea. Rev.*, **110**, 118–135.
- , and —, 1983: Water budget of a mesoscale convective system in the tropics. *J. Atmos. Sci.*, **40**, 1835–1850.
- Gunn, K. L. S., and J. S. Marshall, 1958: The distribution with size of aggregate snowflakes. *J. Meteor.*, **15**, 452–461.
- Houghton, H. G., 1968: On precipitation mechanisms and their artificial modification. *J. Appl. Meteor.*, **7**, 851–859.
- Houze, R. A., Jr., 1977: Structure and dynamics of a tropical squall-line system. *Mon. Wea. Rev.*, **105**, 1540–1567.
- , 1981: Structures of atmospheric precipitation systems: A global survey. *Radio Sci.*, **16**, 671–689.
- , and E. N. Rappaport, 1984: Air motions and precipitation structure of an early summer squall line over the eastern tropical Atlantic. *J. Atmos. Sci.*, **41**, 553–574.
- Jorgensen, D. P., 1984a: Mesoscale and convective-scale characteristics of mature hurricanes. Part I: General observations by research aircraft. *J. Atmos. Sci.*, **41**, 1268–1285.
- , 1984b: Mesoscale and convective-scale characteristics of mature hurricanes. Part II: Inner core structure of Hurricane Allen (1980). *J. Atmos. Sci.*, **41**, 1287–1311.
- , P. H. Hildebrand and C. L. Frusch, 1983: Feasibility test of an airborne pulse-Doppler meteorological radar. *J. Climate Appl. Meteor.*, **22**, 744–757.
- , E. J. Zipser and M. A. Lemone, 1985: Vertical motions in intense hurricanes. *J. Atmos. Sci.*, **42**, 839–856.
- Joss, J., and A. Waldvogel, 1970: Raindrop size distribution and Doppler velocities. Preprint 14th Conference on Radar Meteorology, Tucson, Arizona, published by Amer. Meteor. Soc., 153–156.
- Leary, C. A., 1984: Precipitation structure of the cloud clusters in a tropical easterly wave. *Mon. Wea. Rev.*, **112**, 313–325.
- , and R. A. Houze, Jr., 1979: Melting and evaporation of hydrometeors in precipitation from the anvil clouds of deep tropical convection. *J. Atmos. Sci.*, **36**, 669–679.
- Lhermitte, R. M., and D. Atlas, 1963: Doppler fallspeed and particle growth in stratiform precipitation. Preprints, 10th Conference on Radar Meteorology, Washington, D.C., Amer. Meteor. Soc., 297–302.
- Lord, S. J., H. E. Willoughby and J. M. Piotrowicz, 1984: Role of parameterized ice-phase microphysics in an axisymmetric, non-hydrostatic tropical cyclone model. *J. Atmos. Sci.*, **41**, 2836–2848.
- Marks, F. D., Jr., 1985: Evolution and structure of precipitation in Hurricane Allen (1980). *Mon. Wea. Rev.*, **113**, 909–930.
- , and R. A. Houze, Jr., 1984: Airborne Doppler radar observations in Hurricane Debby. *Bull. Amer. Meteor. Soc.*, **65**, 569–582.
- Nuñez, E., and W. M. Gray, 1977: A comparison between West Indies hurricanes and Pacific typhoons. Reprints of 11th Technical Conference on Hurricane and Tropical Meteorology, Miami Beach, Florida, 528–534.
- Ooyama, K. V., 1982: Conceptual evolution of the theory and modeling of the tropical cyclone. *J. Meteor. Soc. Japan*, **60**, 369–380.
- Pruppacher, H. R., and J. D. Klett, 1978: *Microphysics of Clouds and Precipitation*, D. Reidel, 714 pp.
- Rogers, R. R., 1964: An extension of the Z-R relation for Doppler radar. Preprints of the 11th Conference on Radar Meteorology, Boulder, Colorado, Amer. Meteor. Soc., 158–161.
- Shapiro, L. J., 1983: The asymmetric boundary layer flow under a translating hurricane. *J. Atmos. Sci.*, **40**, 1984–1998.
- , and H. E. Willoughby, 1982: The response of balanced hurricanes to local sources of heat and momentum. *J. Atmos. Sci.*, **39**, 378–394.
- Shea, D. J., and W. M. Gray, 1973: The hurricane's inner core region: I. Symmetric and asymmetric structure. *J. Atmos. Sci.*, **30**, 1544–1564.
- Willoughby, H. E., and M. B. Chelmon, 1982: Objective determination of hurricane tracks from aircraft observations. *Mon. Wea. Rev.*, **110**, 1298–1305.
- , J. A. Clos and M. G. Shoreibah, 1982: Concentric eyes, secondary wind maxima, and the evolution of the hurricane vortex. *J. Atmos. Sci.*, **39**, 395–411.
- , H.-L. Jin, S. J. Lord and J. M. Piotrowicz, 1984a: Hurricane structure and evolution as simulated by an axisymmetric, non-hydrostatic numerical model. *J. Atmos. Sci.*, **41**, 1169–1186.
- , F. D. Marks, Jr. and R. J. Feinberg, 1984b: Stationary and propagating convective bands in asymmetric hurricanes. *J. Atmos. Sci.*, **41**, 3189–3211.